

UV EXCESS MEASURES OF ACCRETION ONTO YOUNG VERY LOW-MASS STARS AND BROWN DWARFS

GREGORY J. HERCZEG¹ & LYNNE A. HILLENBRAND¹

Draft version October 29, 2018

ABSTRACT

Low-resolution spectra from 3000–9000 Å of young low-mass stars and brown dwarfs were obtained with LRIS on *Keck I*. The excess UV and optical emission arising in the Balmer and Paschen continua yields mass accretion rates ranging from 2×10^{-12} to $10^{-8} M_{\odot} \text{ yr}^{-1}$. These results are compared with *HST*/STIS spectra of roughly solar-mass accretors with accretion rates that range from 2×10^{-10} to $5 \times 10^{-8} M_{\odot} \text{ yr}^{-1}$. The weak photospheric emission from M-dwarfs at $< 4000 \text{ Å}$ leads to a higher contrast between the accretion and photospheric emission relative to higher-mass counterparts. The mass accretion rates measured here are systematically $\sim 4 - 7$ times larger than those from H α emission line profiles, with a difference that is consistent with but unlikely to be explained by the uncertainty in both methods. The accretion luminosity correlates well with many line luminosities, including high Balmer and many He I lines. Correlations of the accretion rate with H α 10% width and line fluxes show a large amount of scatter. Our results and previous accretion rate measurements suggest that $\dot{M} \propto M^{1.87 \pm 0.26}$ for accretors in the Taurus Molecular Cloud.

Subject headings: stars: pre-main sequence — stars: planetary systems: protoplanetary disks

1. INTRODUCTION

In the magnetospheric accretion model for accretion onto young stars, the stellar magnetosphere truncates the disk at a few stellar radii. Gas from the disk accretes onto the star along magnetic field lines and shocks at the stellar surface. The $\sim 10^4$ K optically-thick post-shock and optically-thin pre-shock gas produce emission in the Balmer and Paschen continuum and in many lines, including the Balmer and Paschen series and the Ca II IR triplet (Hartmann et al. 1994; Calvet & Gullbring 1998). The accretion luminosity may be estimated from any of these accretion tracers and subsequently converted into a mass accretion rate.

Historically, mass accretion rates onto young stars have been measured directly using optical veiling from the Paschen continuum and stronger Balmer continuum emission shortward of the Balmer jump. Modelling of the Paschen and Balmer continuum emission with a generic isothermal, plane-parallel slab yields $\dot{M} \sim 10^{-7} - 10^{-10} M_{\odot} \text{ yr}^{-1}$ for accretors with masses of 0.4–1.0 M_{\odot} (Valenti et al. 1993; Gullbring et al. 1998). Calvet & Gullbring (1998) obtained similar accretion rates by applying more realistic shock geometries with a range of temperatures to explain the observed accretion continuum. The accretion luminosity can be measured instead at longer wavelengths with optical veiling measurements from high-dispersion spectra (e.g. Basri & Batalha 1990; Hartigan et al. 1991, 1995; Hartigan & Kenyon 2003; White & Hillenbrand 2004), albeit with a larger uncertainty in bolometric correction.

Several deep surveys have since identified large populations of young very low-mass stars and brown dwarfs with masses $< 0.2 M_{\odot}$ (e.g. Briceno et al. 1998; Luhman 2004; Slesnick et al. 2006; Guieu et al. 2007). Excess IR emission indicates the presence of disks around some of these very low-mass objects² (e.g. Muzerolle et al. 2003;

Jayawardhana et al. 2003; Natta et al. 2004). The excess Balmer continuum emission produced by accretion onto very low-mass stars and brown dwarfs has not been observed previously. Instead, accretion has been measured based on magnetospheric models of the H α line profile (Muzerolle et al. 2000, 2003, 2005), by extending relationships between \dot{M} and line luminosities established at higher masses to brown dwarf masses (Natta et al. 2004, 2006; Mohanty et al. 2005), or in a few cases from measurements of the Paschen continuum (White & Basri 2003).

In this paper, we present the first observations of the Balmer jump, and hence direct measurements of the accretion luminosity, for young very low-mass stars and brown dwarfs using data obtained with LRIS on *Keck I*. We compare the Balmer and Paschen continuum emission from very low-mass stars to that from higher-mass accretors that were observed with *HST*. The weak U-band photospheric emission of M-dwarfs leads to a high contrast between accretion and photospheric emission at $\lambda < 3700 \text{ Å}$. The properties of the Balmer continuum and jump for very low-mass stars and brown dwarfs are mostly similar to those of the higher-mass accretors, although the sensitivity to low \dot{M} improves to smaller stellar mass. The Balmer jump tends to be larger for smaller mass accretion rates, indicating lower optical depth for the emitting gas. The luminosity in many lines, including the Balmer series and He I lines, correlate well with the accretion luminosity. Our \dot{M} estimates are systematically $\sim 4 - 7$ times higher than those estimated from modelling the H α line profile. We find that $\dot{M} \propto M^{1.9}$ for accretors in Taurus and discuss biases in the selection of those accretors that may affect this calculated relationship.

2. OBSERVATIONS

² The objects studied in this paper span the mass range from 0.024–0.2 M_{\odot} ; hereafter all are referred to as “stars” for ease of terminology. We refer to $\sim 0.3 - 1 M_{\odot}$ stars as “higher-mass stars.”

¹ Caltech, MC105-24, 1200 E. California Blvd., Pasadena, CA 91125

2.1. *Keck I/LRIS*

We used LRIS (Oke et al. 1995; McCarthy et al. 1998) on Keck I to obtain low-resolution optical spectra covering 3000–9000 Å of 17 young, low-mass Taurus sources and 2M1207-3932 on 23 November 2006. We observed 2M0436+2351 and obtained a deeper observation of 2M1207-3932 on 7 February 2007. Our observation log (Table 1) lists the exposure time for each target and abbreviations for each target used throughout this paper.

Most targets were observed with a $175'' \times 1''0$ slit. The light was split into separate red and blue beams with the D560 dichroic. The red light illuminates a 2048×2048 CCD with $0''.21$ pixels and the blue light illuminates a 2048×4096 CCD with $0''.135$ pixels. We used the 400/8500 grism and the GG495 filter in the red channel and the 400/3400 grism in the blue channel. Each red pixel covers ~ 1.85 Å, yielding a resolution $R \sim 1400$ over the 5400–9000 Å wavelength range. Each blue pixel covers ~ 1.1 Å, yielding a resolution $R \sim 700$ over the 3000–5700 Å wavelength range. For each target we typically obtained multiple red spectra during a 1–2 long blue exposure.

We bias-subtracted the 23 November blue exposures and estimated a bias subtraction for the 7 February 2007 blue exposure from images with no blue emission. An overscan subtraction was applied to all red images. The red images were flat-fielded with dome flats, the blue images from November 2006 were flat-fielded with sky flats, and the blue images from February 2007 were flat-fielded with halogen lamp flats. We located each spectrum on the detector as a function of position in the dispersion direction. The counts in the red and blue spectra were extracted with 11 and 13-pixel widths, respectively. The sky background was measured from nearby windows and subtracted from the spectrum. The spectral regions within 25 Å of 4590 and 5270 Å include a transient ghost and are ignored.

The relative wavelength solution was calculated from a HgNeArCdZn lamp spectrum. The absolute wavelength solution for each observation was calculated by measuring the positions of sky emission lines.

All stars were observed at the parallactic angle. On 23 November the seeing improved from $0''.9$ to $0''.7$ from the beginning to the middle of the night and remained stable at $0''.7$ for the second half of the night. On 7 February the seeing was $0''.7$ during our observation of 2M0436+2351 and $1''.2$ during our observation of 2M1207-3932.

We obtained observations of the spectrophotometric standards (Massey et al. 1988; Oke et al. 1990) PG0205+134 and PG0939+262 at the beginning and end of the November 2006 run and G191B2B and PG1545+035 on February 7 2007 with the $1''0$ aperture. The November 23 standards have published fluxes from 3100–8000 Å. We approximate the flux of PG0939+262 from 8000–9000 Å by assuming that the white dwarf spectrum is a blackbody, and confirm this calibration by comparing the spectra of 2M1207-3932 obtained on both nights. The atmospheric extinction correction was obtained from multiple observations of G191B2B on 7 February 2007.

Slit losses were $\sim 70\%$ at the beginning of the night and $\sim 22\%$ at the end of the night in Nov. 2006. In adjacent red spectra of the same target, the extinction-corrected

count rate increased early in the night and remained stable during the second half of the night, mirroring similar changes in the seeing. This increase in count rate can account entirely for the factor of ~ 3 in slit losses. The count rates in the first half of the night are therefore multiplied by a factor between 1–3, based on when the observation occurred. The small wavelength dependence in this factor is found by interpolating from the observations of the photometric standards.

Table 1 lists synthetic UBVR magnitudes for each source and our estimated uncertainty in absolute flux calibration. The estimated photometry is within 0.1–0.5 mag of most existing literature measurements, with the exception of several strong accretors. The initial flux calibration of 2M1207-3932 on the two nights differed by 0.27 mag. We estimate that the absolute fluxes are calibrated to at worst a factor of 2 early in the night and a factor of 1.3 in the second half of the night for the Nov. 2006 observations.

2.2. *Archival HST Spectra*

We supplement our new *Keck* data with existing blue *HST*/STIS spectra of late-K or early-M accretors and two young non-accretors taken from the MAST archive (see Table 2). The spectra were obtained with the G430L grating and span 2900–5700 Å with a spectral resolution of ~ 600 . Several of these observations were discussed in Herczeg et al. (2004, 2005, 2006), including calculations of the mass accretion rate. We re-analyze these data here to provide a small set of higher-mass accretors with spectra analyzed in a manner consistent with our *Keck I/LRIS* spectra to compare with results from our sample of low-mass accretors.

2.3. *Description of our sample*

Several targets (GM Tau, CIDA 1, 2M0414+2811) in our *Keck I/LRIS* program were selected based on expectation of a high mass accretion rate inferred from strong excess continuum emission and optical line emission. Other targets were selected based on a combination of spectral type, low extinction, existing \dot{M} measurements from H α , and visual magnitude. MHO 5 and KPNO 11 were selected also for a full-width of the H α line at 10% the peak flux (hereafter H α 10% width) of 150–200 km s $^{-1}$ (Muzerolle et al. 2003; Mohanty et al. 2005), which is intermediate between definite accretors and definite non-accretors for their respective spectral types. Three relatively-bright young stars in Taurus were chosen as photospheric templates based on spectral type and lack of strong accretion, as identified by weak H α emission and absence of IR excess emission. Since the template stars are young, their surface gravity will be similar to the rest of the sample and provide a better match to the photospheric spectrum than could be obtained from older field dwarfs.

To obtain a larger range in \dot{M} for analyzing the properties of the accretion continuum and relationships between line and continuum emission (see §5 and 6), we supplemented the *Keck I/LRIS* spectra with *HST*/STIS observations of stars with higher central masses. This sample consists of most available *HST* observations of the 3000–5000 Å region for accreting young stars with spectral types late K or early M.

Table 3 describes the properties of these targets (see also §9). Multiple LRIS observations of 2M1207-3932 and *HST* observations of DF Tau and TW Hya are treated independently throughout this paper.

3. OBSERVATIONS OF ACCRETION DIAGNOSTICS

Figure 1 compares three M5-M5.5 stars in our *Keck*/LRIS spectra from 3200–5600 Å. Strong TiO and CaH molecular bands (Kirkpatrick et al. 1993) dominate the photospheric emission of mid-M dwarfs. At > 3700 Å, such features are strong from V927 Tau and S0439+2336 but shallow from S0518+2327. This veiling of the photospheric emission from S0518+2327 is attributed to excess Paschen continuum emission. S0439+2336 and S0518+2327 both exhibit strong excess emission shortward of jump at 3700 Å, which is attributed to excess Balmer continuum emission. Line emission, including in the Balmer series, is much stronger from S0439+2336 and S0518+2327 than from V927 Tau. The excess Balmer and Paschen continuum and emission lines detected from young stars are commonly attributed to accretion. In the following subsections we describe and measure these accretion diagnostics for each source.

3.1. Measuring the Paschen Continuum

Veiling³ is measured by comparing the depth of absorption features, which are filled in by emission from the accretion continuum, to photospheric templates. These features include the TiO and CaH absorption bands and also the strong Ca I λ 4226 absorption line. The Ca I line depth may be related to chromospheric structure and may be affected by stellar rotation (Mauas & Falchi 1996; Short et al. 1997).

The young M-dwarfs V927 Tau (M5), MHO 7 (M5.5), CFHT 7 (M6.5) and 2M0439+2544 (M7.25) serve as photospheric templates (see §9.1). These stars provide a better match to the surface gravity and chromospheric emission of young accretors than would older field M-dwarfs. 2M0439+2544 is not an ideal template because of ongoing accretion, and V927 Tau may also be accreting (see §3.4 and §9.4.2). Use of 2M0439+2544 and V927 Tau as templates may cause us to underestimate the veiling by 0.05 and 0.02, respectively, at 5000 Å and 0.01 each at 7000 Å. At < 4500 Å we use CFHT 7 instead of 2M0439+2544 as a photospheric template for late M-stars.

Large veilings ($\gtrsim 2$) are difficult to measure because the high ratio of accretion-to-photospheric flux masks any photospheric absorption features. However, a large error for a high value of veiling leads to only a small error in the measurement of the underlying continuum flux. Our lower detection limit of veiling measurements is $\sim 0.05 - 0.1$, depending on how well the photospheric template matches the spectrum. The veiling is calculated from regions that do not include obvious strong emission lines. For weaker accretors, any such lines may fill in some of the absorption and thereby artificially increase our veiling estimate for some stars, particularly at 4227 Å (see Fig. 2).

Figures 2–4 show three spectral regions where veiling is measured. Table 4 lists veiling measurements and the

³ The veiling at wavelength λ , r_λ , is defined by the accretion continuum flux ($F_{\text{observed}} - F_{\text{photosphere}}$) divided by the photospheric flux.

corresponding flux in the accretion continuum at distinct wavelengths between 4000-9000 Å. Excess continuum emission is detected longward of 4000 Å for many stars in our sample and is identified as the Paschen continuum. The accretion continuum is relatively flat at < 6000 Å for most targets, and increases at $\lambda > 6000$ Å for most sources where it is detected. The continuum flux from 2M0414+2811 at 8600 Å is substantially lower than that at 7800 Å, which may be consistent with weaker Brackett continuum emission longward of the Paschen jump. CIDA 1 shows no such flux reduction, which may suggest an alternate veiling source.

The early-M and late-K stars from the STIS data do not have the strong TiO and CaH absorption bands for veiling measurements. In several locations, the photospheric emission drops by a factor of 2–2.5 within ~ 200 Å. Table 5 list veilings at 4600 and 5400 Å for this sample, measured by comparing the depth of these features with photospheric templates, and at 4000 Å, measured from the slope of the photospheric emission. We detect Paschen continuum emission from DF Tau, TW Hya, V836 Tau, DG Tau, and RU Lup.

3.2. Measuring the Balmer Continuum

When seen from young stars, excess Balmer continuum emission shortward of ~ 3700 Å is typically attributed to accretion (Figure 5). The Balmer limit occurs at 3646 Å, but line blending in the Balmer series shifts the apparent jump to 3700 Å. The observed Balmer jump, defined here as the ratio of flux at 3600 Å to the flux at 4000 Å, ranges from ~ 0.35 for the non-accretors to 5.47 for the accretor 2M1207-3932 (Table 6).

Figure 6 compares spectra of stars with the weakest Balmer jumps in our sample to that of photospheric templates from Table 4. Excess Balmer continuum emission is clearly detected from 2M0455+3028, S0439+2336, and V927 Tau relative to photospheric templates. Some weak, noisy Balmer continuum emission is also detected from MHO 5 and KPNO 11. MHO 7 and CFHT 7 may each show very mild increases in emission shortward of the Balmer jump, possibly from chromospheric emission (see §3.4).

As defined here, the Balmer jump is the ratio of Balmer plus Paschen continuum flux at 3600 Å divided by the Paschen continuum flux at 4000 Å. The intrinsic Balmer Jump (J_{mod} in Table 6) is measured from the accretion continuum after dereddening the spectra (see §9.2) and subtracting a scaled photospheric spectrum. Table 6 also lists the measured slope of the continuum emission from 3200–3650 Å (S_B), scaled to the observed flux at 3600 Å.

3.3. Emission Line Measurements

Tables 7–10 list equivalent widths and fluxes for H Balmer lines, He lines, other strong lines associated with accretion, and lines usually associated with outflows.⁴ These tables are not complete linelists. We measure most emission line fluxes and equivalent widths by fitting a Gaussian profile to the observed line. The focus was poor at $\lambda > 8000$ Å and produced asymmetric emission lines. Line strengths in that spectral region are measured by summing the flux across a continuum-subtracted window that includes the entire line. The Balmer and Ca II

H & K lines are bright from every source and are measured directly from the spectra. For all other lines we subtract a scaled photospheric template to increase our sensitivity to small fluxes. These line equivalent widths and corresponding fluxes are relative to the photospheric template and may be offset by a small amount in equivalent width if line emission is present but undetected in the photospheric template. This method may also yield false weak detections if the depth of Na I or Ca II photospheric absorption features differ substantially from star-to-star. Weak Ca II IR triplet emission from several targets is only treated as real if all three of the lines are detected, unless the non-detection has a large upper limit on equivalent width. Our detection limits typically range from $\sim 0.1 - 1.5 \text{ \AA}$, depending on the match with a photospheric template and the signal-to-noise. The equivalent widths in low-resolution spectra are affected by absorption and may differ from equivalent widths measured in high-resolution spectra because of different spectral regions used to calculate the continuum emission.

The sources with strongest veiling also show the strongest line emission. For example, Ca II IR triplet emission is detected from only CIDA 1, 2M0414+2811, GM Tau, 2M0441+2534, and S0518+2327. Similarly, the Paschen series is detected from only CIDA 1, 2M0414+2811, and GM Tau. Several Paschen lines blend with and contribute $\leq 10\%$ of the flux in the Ca II IR triplet lines. Other lines, including the Na I D doublet, He II $\lambda 4686$, and He I lines are detected from most stars with excess Balmer emission.

Optical forbidden lines, including the [O I] $\lambda 6300, 6363$, [S II] $\lambda 6716, 6731$, and [S I] $\lambda 4069, 4076$ doublets, are detected from many sources. [N II] $\lambda 6584$ is detected from 2M0444+2612 but is difficult to resolve from the bright H α emission for many other stars in the sample. The [O I] lines are unresolved in the cross-dispersion direction, which constrains the emission to have a FWHM of $< 0.2 - 0.3$.

3.4. Designation of Accretors from the Balmer continuum

Many emission line diagnostics have been used to identify accretion onto young very low-mass stars and brown dwarfs. An H α equivalent width of $> 10 \text{ \AA}$ is the traditional criterion above which a young star is classified as an accretor. Against the weaker photospheric continua of redder M-dwarfs, chromospheric emission can produce H α emission with equivalent widths larger than 10 \AA . In lieu of this diagnostic, the full-width at 10% the peak emission in the H α line has been used to diagnose accretion, with values greater than $180-200 \text{ km s}^{-1}$ indicating accretion for very low-mass stars (e.g. White & Basri 2003; Muzerolle et al. 2003; Natta et al. 2004; Mohanty et al. 2005). Accretion onto low-mass stars has also been identified by emission in permitted optical lines. Optical forbidden lines are produced by outflows and can therefore be used as indirect accretion diagnostics because outflows require ongoing or recent accretion (e.g. Hamann et al. 1994; Hartigan et al. 1995). The presence of excess Balmer and Paschen continuum emission is also associated with accretion (e.g. Valenti et al. 1993; Gullbring et al. 1998). In this subsection we describe the Balmer jump and excess Balmer continuum emission as an accretion diagnostic for the

individual stars in our sample. In general, the classification of stars as accretors or non-accretors based on the presence or absence of Balmer continuum emission is consistent with previous classifications using alternate accretion diagnostics.

Two mid-M dwarfs in our sample, CFHT 7 and MHO 7, were previously classified as non-accretors. For CFHT 7, Guieu et al. (2007) measured only weak H α emission and found an absence of excess IR emission shortward of and including the *Spitzer* $24\mu\text{m}$ MIPS bandpass. For MHO 7, Muzerolle et al. (2003) measured weak H α emission with a 10% width of 115 km s^{-1} and no excess K-band emission. These two stars have Balmer jumps of 0.36 and 0.34, respectively. Both stars are chromospherically active, with equivalent widths in Ca II H & K and He I lines that are larger than is typically measured from chromospheres of older, magnetically-active M-dwarfs (e.g. Giampapa et al. 1982; Gizis et al. 2002; Rauscher & Marcy 2006; Allred et al. 2006). The earlier-type non-accretors LkCa 7 and V819 Tau are bluer and have Balmer jumps of 0.44 and 0.46, respectively.

Many stars in our LRIS sample have much larger observed Balmer jumps than those non-accretors. The stars GM Tau, CIDA 1, 2M0414+2811, 2M0441+2534, and S0518+2327 have Balmer jumps ranging from 2.0–3.4 and excess Paschen continuum emission detected at $> 6000 \text{ \AA}$. These stars are also associated with strong emission in the Balmer series, He I lines, the Ca II IR triplet, O I $\lambda 7773, 8446$, and many forbidden lines

The stars MHO 6, 2M0439+2544, 2M0444+2512, S0439+2336, 2M0436+2351, and 2M1207-3932 have excess Paschen continuum emission detected at 4227 \AA but not at $> 5500 \text{ \AA}$, and five have Balmer jumps between 0.7–1.4. The two observations of 2M1207-3932 yield outlier Balmer jumps of 3.9 and 5.7. These six targets are associated with some strong permitted line emission, including bright Balmer continuum emission and He I line equivalent widths of $> 1 \text{ \AA}$, and some forbidden line emission. Any Ca II IR triplet emission is faint.

Each of these stars can be identified as accretors based on their high Balmer jump. Similarly, the higher-mass stars TW Hya, DF Tau, RU Lupi, and DG Tau have Balmer jumps that are well above that of non-accretors and can be classified as accretors based on either the Balmer jump or the presence of bright emission lines. As with other diagnostics, small Balmer jumps with values near those of non-accreting templates may be inconclusive for classifying stars as accretors. V836 Tau has an observed Balmer jump of 0.60, which is higher than non-accretors with similar spectral type. Many young late K and early M stars that are not identified with accretion show no signs of excess Balmer continuum emission. Thus, this excess emission from V836 Tau is identified as a clear indication of accretion.

MHO 5, 2M0455+3028, CIDA 14, KPNO 11, and V927 Tau all have observed Balmer jumps consistent with or slightly above the non-accretors. Figure 6 shows that some excess Balmer emission relative to photospheric templates is present from each of these stars, with veiling at 3600 \AA that range from 0.14–0.54 (see Table 11). Emission line diagnostics suggest that MHO 5, CIDA 14, and V927 Tau are actively accreting (see §9.4), while the status of 2M0455+3028 and KPNO 11 is uncertain from other diagnostics.

The weak excess Balmer continuum emission from these five stars could in principle be produced by the stellar chromosphere. Younger M-dwarfs are bluer and more chromospherically active than older M-dwarfs (Cardini & Cassatella 2007), which is consistent with enhanced Balmer and Paschen continuum emission. However, the Balmer jump and elevated Balmer continuum emission is not detected during stellar flares (Hawley & Pettersen 1991; Eason et al. 1992), which may suggest that stellar chromospheres do not produce any Balmer continuum emission. In this case, any weak excess emission could be attributed to accretion. A larger sample of U-band spectra from non-accreting young M-dwarfs is needed to definitively rule out a chromospheric origin. For the remainder of the paper we treat the excess emission from these five stars as upper limits. We also suggest the criterion that any observed Balmer jump of > 0.5 for a mid-M dwarf should be considered an accretor.

4. MASS ACCRETION RATES

4.1. *Description of Accretion Models*

The accretion emission consists of a strong Balmer continuum, a weaker Paschen continuum, and many lines. The flux in the accretion continuum is measured for the entire 3000–9000 Å wavelength range from only the strongest three accretors (see Table 4). For the weakest accretors the veiling is measurable only shortward of the Balmer jump. Calculating the total luminosity of the accretion shock requires modelling the observed accretion SED to obtain a bolometric correction that accounts for unseen emission.

The H Balmer and Paschen continua and series can be approximated by an isothermal, plane-parallel, pure hydrogen slab model following Valenti et al. (1993) and Gullbring et al. (1998). These simplistic models were developed based on the outdated boundary layer accretion paradigm but are robust to different geometries for the emitting gas. We use these isothermal plane-parallel model from Valenti et al. (1993) because it does not rely on a specific morphology of the accretion flow and it provides measurements of the accretion luminosity calculated with a methodology consistent with Valenti et al. (1993) and Gullbring et al. (1998).

The accretion slab models of Valenti et al. (1993) approximate the broadband hydrogen accretion continuum with the following free parameters: temperature T , density n_e , path length L of the emitting gas (an opacity parameter), turbulent velocity, and filling factor δ of the accretion slab. At low density ($n_e < 10^{13} \text{ cm}^{-3}$) the Balmer jump is large and determined by the temperature of the emitting gas. At higher density stronger H^- continuum emission reduces the size of the Balmer jump and makes the continuum shape at $< 3700 \text{ Å}$ bluer. The Balmer and Paschen continua become redder and the size of the Balmer jump increases with decreasing temperature, while both continua become bluer and the size of the Balmer jump decreases with increasing optical depth (n_e and L). In our fits we vary the temperature, density, and path length while setting the turbulent velocity to $\sim 120 \text{ km s}^{-1}$, which is smaller than the 150 km s^{-1} used by Valenti et al. (1993). Larger turbulent velocities yield Balmer line profiles that are broader than is observed. Substantially smaller turbulent velocities are

unable to reproduce the shoulder of the Balmer jump, located between the real Balmer jump at 3646 Å and the observed Balmer jump at $\sim 3700 \text{ Å}$, that is attributed to blending of high Balmer lines. The synthetic spectrum is then scaled to the measured flux accretion continuum. The filling factor of the emission on the stellar surface is calculated from the accretion luminosity and temperature.

Calvet & Gullbring (1998) developed more advanced models of the pre- and post-shock gas at the footpoint of the magnetospheric accretion column on the star. In their models the Balmer continuum is produced in the optically-thin pre-shock gas while the Paschen continuum is produced in the optically-thick post-shock gas. The optically-thin pre-shock gas has an intrinsically large Balmer jump. The optically-thick post-shock region has a high density and small Balmer jump. The observed Balmer jump is therefore not density-sensitive but instead depends on the relative amount and temperature of the pre- and post-shock gas. Our primary goal for modelling the measured accretion continuum is estimating bolometric corrections to convert the continuum flux to an accretion luminosity. Calvet & Gullbring (1998) find that the two model variants lead to 2–5% differences in the slope of the Balmer continuum and 5–10% differences in the slope of the Paschen continua, so that the continuum emission from shock models is redder. However, our models and the models of Calvet & Gullbring (1998) both successfully explain continuum emission at $< 5600 \text{ Å}$ and both underestimate continuum emission at $> 6000 \text{ Å}$ (see §4.2). We therefore suggest that any differences between the two models in the bolometric correction are modest.

4.2. *Application of Models to the Observed Spectra*

We fit the synthetic accretion spectrum plus a photospheric template to the unreddened blue spectra between 3200–5600 Å. The photospheric template is scaled to match our estimate for photospheric emission between 3200–5600 Å, which is informed by veiling estimates (see Tables 4–5).

The stars with measurable accretion continuum emission longward of the Balmer jump allow us to constrain some parameters of the plane parallel slab. Figure 7 shows that the slope of the Balmer continuum constrains T while the Balmer jump constrains n_e . Values of T and n_e for each star are adopted from the center of the acceptable contours, with L is subsequently tuned to match the strength of the high Balmer lines. Since L and n_e are not independent, a lower L may be consistent with a larger n_e . In several cases L could not be tuned to yield the observed flux in the high Balmer lines. In the context of the Calvet & Gullbring (1998) shock models, the larger Balmer jump may be caused instead by fainter Paschen continuum emission from the optically-thick post-shock gas relative to the Balmer continuum from the optically-thin pre-shock gas.

The lower Balmer lines are easily affected by emission or absorption in the wind and are consistently underestimated by our models. In magnetospheric accretion models of Muzerolle et al. (2001) and Kurosawa et al. (2006), emission in the Balmer lines is dominated by the funnel flow. If the high Balmer lines are also produced in the accretion flow, then the slab optical depths in our models

should be larger. The slab optical depth may be smaller if instead the wind is optically thick and absorbs a large percentage of emission in all of the Balmer series lines.

The stars S0439+2336, 2M0455+3028, MHO 5, CIDA 14, KPNO 11, and V836 Tau have weak Balmer continuum emission and undetected Paschen continuum emission. Since the size of the intrinsic Balmer jump for these targets is uncertain, we assume values for n_e , T , and l based on our other data. We adjust the parameters to match the synthetic Balmer series and scale the emission so that the spectrum of a photospheric template plus accretion matches the total emission spectrum.

Table 11 lists approximate accretion slab parameters for each star, the estimated Balmer jump of the accretion continuum, the slope of the Balmer continuum, the veiling at 3600 and 4000 Å measured from these fits, and the total accretion slab luminosity. The continuum emission from each target is well characterized by temperatures of $\sim 7000 - 9500$ K, densities of $(0.3 - 2) \times 10^{14}$ cm $^{-3}$ and lengths of $\sim (0.5 - 50) \times 10^7$ cm. In Figure 8 we show our fits to each spectrum. The synthetic hydrogen continuum is consistent with veiling measurements at < 5600 Å but underestimates the veiling at > 6000 Å from 2M0414+2811, 2M0441+2534, CIDA 1, GM Tau, and S0518+2327 by a factor or 1.2–2. The intrinsic Balmer jump of 2M1207-3932 (15 ± 4 and 7 ± 2 for our two observations) is particularly large, which indicates a low H $^-$ opacity. A few outliers in the Valenti et al. (1993) and Gullbring et al. (1998) data also have large Balmer jumps.

4.3. Calculating Mass Accretion Rates and Errors

The accretion luminosity, L_{acc} , can be converted to the mass accretion rate, \dot{M} , by assuming that the accretion energy is reprocessed entirely into the accretion continuum. The mass accretion rate is then

$$\dot{M} = \left(1 - \frac{R_*}{R_{in}}\right)^{-1} \frac{L_{acc} R_*}{GM_*} \sim 1.25 \frac{L_{acc} R_*}{GM_*} \quad (1)$$

where the factor $(1 - \frac{R_*}{R_{in}})^{-1} \sim 1.25$ is estimated by assuming the accreting gas falls onto the star from the truncation radius of the disk, $R_{in} \sim 5 R_*$ (Gullbring et al. 1998). The stellar mass and radius are listed in Table 3 (see also §9.3). We calculate mass accretion rates between 2×10^{-12} to $10^{-8} M_\odot \text{ yr}^{-1}$ for the very low-mass stars and brown dwarfs in our *Keck*/LRIS sample and $2 \times 10^{-10} - 5 \times 10^{-8} M_\odot \text{ yr}^{-1}$ in the *HST*/STIS sample of higher-mass stars (Table 11).

The parameters in Equation 1 suffer from systematic and random uncertainties related to the data itself, interpretation of the data, and geometrical assumptions. In the following subsections and in Table 12, we describe for purposes of explicit clarity these sources of uncertainty and how they affect our measurements of \dot{M} .

4.3.1. Errors in Assumed Stellar Properties

Distance enters into calculations of \dot{M} (Eqn. 1) because $L_{acc} \propto d^2$ and $R \propto d$, yielding $\dot{M} \propto d^3$. Based on the kinematic distances calculated by Bertout & Genova (2006), the distance to any individual Taurus member can differ by ~ 15 pc from the standard 140 pc distance (Kenyon et al. 1994)⁵. The $\sim 11\%$ distance uncertainty

in Taurus leads to a 0.13 dex in \dot{M} . The actual deviation in distance may not be random for our Taurus sample because the selection of targets here and in previous work is influenced by the optical brightness. Targets located in front of the cloud will be brighter because of a smaller distance modulus and lower extinctions.

Extinction also affects measures of L_{acc} and R . The adopted 0.5 mag uncertainty in A_V (see §9.2) leads to a 0.32 dex uncertainty in L_{acc} and a 0.08 dex uncertainty in R for a total of 0.4 dex uncertainty in \dot{M} . If $R_V > 3.1$, then the extinction curve would be flatter and our A_V would be underestimated.

The \dot{M} measurements also depend on the ratio $\frac{R}{M}$, which is calculated from the effective temperature and theoretical evolutionary tracks (§9.3). The temperature is uncertain by ~ 75 K, including both the uncertainty of roughly 0.5 spectral type subclasses and the conversion of spectral type to temperature (§9.1). In the Baraffe et al. (1998) pre-main sequence evolutionary tracks at 2 Myr and with temperatures from Luhman et al. (2003), a difference of 0.5 spectral classes corresponds to 25% larger mass and a 10% smaller radius. Alternate pre-main sequence evolutionary tracks from D’Antona & Mazzitelli (1998) would increase our mass estimates 1.1–1.7 times larger than the Baraffe et al. (1998) tracks. White & Hillenbrand (2004) suggest that evolutionary tracks underestimate stellar masses by 30–50%.

All sources except V927 Tau and DF Tau are assumed to be single. If any sources are binaries, the lower luminosity per star would imply that we have overestimated R . The shallower potential well would result in \dot{M} being 1.4 times lower than is calculated here. In cases where both sources are accretors, the accretion luminosity and mass accretion rate is the total rate onto both stars.

4.3.2. Uncertainty in Bolometric Corrections

Converting the measured accretion flux into an accretion luminosity requires a bolometric correction for unseen emission (§4.2). However, the shape of the broadband accretion continuum is not well understood. Our single-temperature slab models underestimate the veiling at 6000 – 9000 Å by factors of 1.2–2, as which also occurs for the multi-temperature shock models (Calvet & Gullbring 1998). The veiling at even longer wavelengths (e.g., White & Hillenbrand 2004; Edwards et al. 2006) also seems larger than can be explained by the isothermal slab that fits well the Balmer continuum and short-wavelength Paschen continuum.

If we hypothetically double the accretion continuum flux at $\lambda > 6000$ Å, the total accretion luminosity increases by 0.15 dex. If instead the flux per Å is constant between 6000–20000 Å (despite the presumed presence of the Paschen jump), then the accretion luminosity increases by 0.3 dex. A smaller uncertainty of ~ 0.1 dex in L_{acc} is introduced by the uncertainty in temperature ($\sim 1000 - 2000$ K) of the plane-parallel slab.

4.3.3. Exclusion of line emission

Our \dot{M} estimates rely on accurate calculations of the total accretion energy that escapes from the shock. Such emission is seen in both continuum and line emission, but we include only the total continuum emission from the

accretion slab in estimating L_{acc} . The observed Balmer line fluxes (Table 7) total 0.2 times L_{acc} for most of the accretors but are roughly equivalent to L_{acc} for the M7-M8 accretors (see Tables 7 and 11). The formation of and flux in lower Balmer lines is complicated by emission and absorption in the accretion funnel flow and in outflows. In principle other lines (e.g., Ca II IR triplet, Lyman series, FUV and X-ray lines) may also need to be included. For TW Hya, X-ray and UV lines account for $\sim 30 - 45\%$ of the total accretion flux, most of which is in H I Ly α , but most have fluxes that when summed are likely $< 20\%$ of the accretion flux (Kastner et al. 2002; Herczeg et al. 2004). Our exclusion of line emission from the accretion luminosity is consistent with previous L_{acc} estimates and is essential for simplifying these calculations and comparisons with existing \dot{M} estimates.

4.3.4. Geometric assumptions

In the magnetospheric accretion paradigm, gas accretes from the inner disk truncation radius, R_{in} , onto the star along magnetic field lines, where R_{in} is determined by where the magnetic field intercepts the disk. Gullbring et al. (1998) noted that infall energy depends on R_{in} and therefore included the factor of $(1 - \frac{R_*}{R_{in}})$ in Equation 1. The R_{in} ranges from 3–10 R_* based on magnetic field strengths of higher-mass CTTSs (Johns-Krull 2007). We assume $R_{in} = 5R_*$ for all targets in this sample for consistency with the same assumption made by Gullbring et al. (1998). A factor of 2 error in $\frac{R_*}{R_{in}}$ leads to a $\sim 0.05 - 0.12$ dex error in the mass accretion rate.

As the gas accretes along the magnetic field lines and shocks at or near the stellar photosphere, some of the emission from the hot spot will be directed at the star. We follow Valenti et al. (1993) and Gullbring et al. (1998) in assuming that all of the accretion energy escapes from the star as hydrogen continuum emission. By this assumption, any accretion emission directed at the star is either coherently re-radiated by the star or provides some heating to the nearby gas, which then cools by hydrogen continuum emission. Hartigan et al. (1995) and Hartigan & Kenyon (2003) instead assumed that half of the Balmer and Paschen continuum emission is absorbed by the star, which increases the calculated \dot{M} by a factor of two. The accretion luminosity may also not be isotropic.

The accretion hot spot is assumed to be the source for all Balmer and Paschen continuum emission from our sample. No excess emission is seen in a sample of non-accreting K-dwarfs that serve as templates for the higher-mass accretors discussed here. Thus, the weak excess Balmer emission from V836 Tau that is attributable to accretion can be accurately measured. Whether the faint excess Balmer emission from 2M0455+3028, CIDA 14, MHO 5, KPNO 11, and V927 Tau is produced by accretion or may be chromospheric is uncertain. Using V927 Tau as a template may lead us to underestimate the upper limit of \dot{M} onto 2M0455+3028 by 0.2 dex. Weak Balmer continuum emission in the template spectrum has a negligible effect for targets with larger L_{acc}/L_{bol} .

4.3.5. Cumulative Effect of Uncertainties on Estimates of Mass Accretion Rates

The uncertainty in bolometric correction, exclusion of emission lines, and the re-radiation of H Paschen and Balmer continuum emission by the star can only increase the estimated accretion rate, while the uncertainty in binarity and pre-main sequence tracks can only decrease the estimated accretion rate. When combined, these errors suggest that our accretion rates have a relative uncertainty of ~ 0.6 dex and underestimate the accretion rate by a factor of 1.2 (or 2.4, if one assumes no re-radiation of the accretion luminosity by the central star).

This error analysis is not a rigorous assessment of the uncertainty in \dot{M} at a specific confidence interval. The uncertainty differs for various targets depending on the accuracy of stellar parameters, and for many targets the error is dominated by uncertainty in A_V . For 2M1207-3932, which has an accurate $A_V = 0$, the \dot{M} is likely underestimated by a factor of 2 (or 4, if the accretion emission is not re-radiated), primarily because we exclude line emission in calculating \dot{M} . The standard deviation of ~ 0.3 dex about this factor of 2 is dominated by systematic uncertainties in the bolometric correction. Systematic uncertainties of this magnitude are also present in all previous UV-excess or optical veiling estimates of \dot{M} . Several uncertainties, including in the extinction measurements, could be reduced with the addition of near-UV spectra, better photospheric templates across the entire wavelength region, a better understanding of veiling at long wavelengths.

Intrinsic variability in accretion rate can also affect non-simultaneous observations. Valenti et al. (2003) describe variability of near-UV emission in repeated *IUE* spectra of young stars. The average near-UV variability is 29% for the 15 K1-M2 accretors that were observed at least 5 times with *IUE*. The near-UV emission from these stars is dominated by and should correlate directly with the accretion rate (Gullbring et al. 2000). Variability of 0.1–0.2 dex is also commonly seen in repeated veiling measurements of DF Tau, TW Hya, and AA Tau (Johns-Krull & Basri 1997; Batalha et al. 2002; Bouvier et al. 2007). Scholz & Jayawardhana (2006) confirm that variability in accretion rate is also seen for brown dwarfs. We infer that the accretion rate is variable by ~ 0.2 dex.

5. RELATIONSHIPS BETWEEN LINE AND CONTINUUM ACCRETION DIAGNOSTICS

The Balmer continuum can be difficult to detect because of large extinctions or instrument limitations. Other accretion diagnostics are therefore usually more accessible and can be used to infer accretion rates. In the following subsections we derive and evaluate empirical relationships between emission lines and accretion luminosities and rates. In §5.1 we calculate accretion rates from published data to incorporate additional objects in our analysis in §5.2–5.4. We then compare the accretion luminosity and resulting accretion rate with H α line profile measures of accretion (§5.2), line luminosities (§5.3), and line surface fluxes (§5.4).

5.1. Calculating accretion luminosity from optical veiling measurements

Although ours are the first Balmer jump measurements of young brown dwarfs, detections of excess Paschen

continuum emission have been published. Calculating \dot{M} from these objects increase the overlap of \dot{M} measured using excess continuum emission and H α line profile modelling (§5.2). Kraus et al. (2006) use broadband *HST* photometry to measure excess V-band emission from several young brown dwarfs. The V-band excess is significant when $r_V > 1.3$, which restricts usage to high mass accretion rates relative to the given stellar mass. We use $\log L_{acc} = -29.59 + \log F_{5450}$ (calculated from Tables 4 and 11) to measure \dot{M} of $10^{-9} - 10^{-11} M_{\odot} \text{ yr}^{-1}$ for GM Tau, KPNO-Tau 4, KPNO-Tau 6, and KPNO-Tau 12 (Table 13). The \dot{M} from GM Tau based on V-band excess is nearly identical to that measured more directly from our low-resolution optical spectra. However, the true \dot{M} was likely 20% larger during the *HST* observation because the V-band excess was ~ 0.2 mag brighter than was estimated here.

Hartigan & Kenyon (2003) analyzed *HST*/STIS spectra of binaries with early M spectral types and masses mostly within the $\sim 0.25 - 0.55 M_{\odot}$ range, including veiling measurements at 6100 Å and luminosities in [O I] $\lambda 6300$, H α , and Ca II $\lambda 8542$ lines. Using $\log L_{acc} = -29.67 + \log F_{6190}$ calculated empirically from our *Keck* I/LRIS spectra (see Tables 4 and 11), we find L_{acc} that are 0.28 – 0.75 times those calculated by Hartigan & Kenyon (2003). We adopt these lower L_{acc} for further analysis.

5.2. Comparing UV-excess Accretion Rates to H α Line Profile Models

Strong H α emission is usually attributed to accretion. At high-resolution the line profile often includes P-Cygni, inverse P-Cygni, or self-reversed absorption that corrupts equivalent width measurements (e.g. Reipurth et al. 1996; Muzerolle et al. 2003). Muzerolle et al. (1998, 2001) applied magnetospheric accretion models to calculate the formation and radiative transfer of H α lines. These models treat the line profile, scaled by stellar parameters, as a proxy for \dot{M} . Muzerolle et al. (2003, 2005) applied these models to very low-mass stars and brown dwarfs to estimate accretion rates. Figure 9a and Table 14 compare mass accretion rates for stars with \dot{M} measured from both H α line profile models and UV-excess measurements.

The UV excess accretion rate measurements are ~ 0.84 dex larger than the H α accretion rate measurements with a standard deviation of 0.3 dex, if MHO 5 and CIDA 14 are ignored. If both the H α and weak excess Balmer emission from those two stars are attributable to accretion, then the UV excess measures are 0.6 dex larger than the H α accretion measures but with a larger (0.5 dex) source-to-source variation.

This difference is consistent with the systematic methodological differences between the two methods. However, that the systematic errors are in opposite directions for the two methods is unlikely. For the UV excess method several uncertainties (see §4.3) would serve to increase our \dot{M} estimates and therefore the discrepancy between the two methods. The uncertainty in the H α \dot{M} calculations of $\sim 3 - 5$ are dominated by uncertainty in the disk truncation radius of the inner disk, assumed to be $2.2 - 3 R_*$ (Muzerolle et al. 2003). The model H α line

width is proportional to $M_*^{0.5}$, so overestimating M_* will lead to underestimating \dot{M} for both methods. Intrinsic variability in \dot{M} can explain much of the scatter once the systematic variation between these two methods is corrected.

In the Muzerolle et al. H α line profile models, the accretion rate is estimated from the line profile along with the stellar mass and disk inclination. Although \dot{M} is correlated with the H α line width in the models, different \dot{M} may vary by more than an order of magnitude for equivalent 10% widths (see also Kurosawa et al. 2006). Natta et al. (2004) found an empirical relationship between \dot{M} and H α 10% width, which is used in the absence of H α line profile modelling. We find a 0.86 dex scatter between the \dot{M} measured here from UV excess and \dot{M} from the Natta et al. (2004) H α relationship (Fig. 9b) and a similar amount of scatter for a similar best-fit line⁴ from Table 15. 2M1207-3932 is a particular outlier on this plot, with an \dot{M} estimated from the H α 10% width that is two orders of magnitude larger than that measured from the UV excess.

5.3. Empirical relationships between line and continuum luminosities

In §3.4 we qualitatively describe that excess continuum and line emission are produced by accretion processes. Lines from accretors exhibit a wide range of profiles in high-resolution spectra, with equivalent widths that are correlated with veiling (e.g. Hamann & Persson 1992; Batalha et al. 1996; Muzerolle et al. 1998; Beristain et al. 2001; Mohanty et al. 2005). Figure 10 shows that the luminosity in many lines (L_{line}) is tightly correlated with accretion continuum luminosity, although this relationship does not require that the emission lines and continuum are produced by the same gas. We improve the fits for the H α , [O I] $\lambda 6300$, and Ca II $\lambda 8542$ lines by supplementing our data with results from Hartigan & Kenyon (2003). All line and accretion luminosities used in this subsection were measured from simultaneous data.

Linear fits of the relationship between $\log L_{acc}$ and $\log L_{line}$ are calculated using the statistical package *asurv* (Feigelson & Nelson 1985), with upper limits ignored (see Table 15 and Figure 10). Most upper limits are not significant and their inclusion does not substantially change the results. 2M0455+3028, KPNO 11, CIDA 14, MHO 5, or V927 Tau (squares in Figure 10) are not included in these fits because the source of the excess Balmer emission is uncertain. For several lines at > 5600 Å, the high \dot{M} range for these fits is dominated by CIDA 1 and GM Tau, both of which have large uncertainty in A_V and therefore \dot{M} . The fits based on few data points should be used with caution.

The H α - L_{acc} correlation has more scatter than the correlation between higher Balmer lines and L_{acc} because the larger oscillator strength of H α can lead to stronger wind absorption. The Balmer and Ca II H & K line lu-

⁴ We find that $\dot{M} = -14.0 + 0.014(\text{H}\alpha \text{ 10\% width})$ from the data in Table 14, excluding upper limits, and $\dot{M} = -12.6 + 0.010(\text{H}\alpha \text{ 10\% width})$ if we combine this data with additional \dot{M} calculated from the Ca II $\lambda 8662$ line fluxes from Mohanty et al. (2005, see also §5.4).

minosities from KPNO 11, 2M0455+3028, MHO 5, and CIDA 14 lie above the linear fit to accretion luminosity. Since these four stars are tentative weak accretors, such line emission is likely produced by the chromosphere. The relationship between the Balmer and Ca II K lines and the accretion luminosity derived from our data is consistent with the results from Gullbring et al. (1998). The luminosities in these lines are systematically ~ 0.5 dex lower in the Valenti et al. (1993) sample than in the Gullbring et al. (1998) sample.⁵ The nature of this discrepancy is not known.

A large amount of scatter in the relationship between [O I] line luminosity and accretion luminosity arises because the [O I] emission line forms in an accretion-powered outflow (Hamann et al. 1994; Hartigan et al. 1995). The comparison of the Hartigan & Kenyon (2003) sample and our sample may be corrupted because [O I] emission is typically spatially-extended (e.g. Hartigan et al. 2004). Any extended [O I] emission could lie outside the narrow $0''.2$ slit width used by (Hartigan et al. 1995), but our $1''.0$ slit width includes any forbidden line emission related to the star. The outflow line luminosities are correlated with accretion rate, though strong accretors sometimes drive weak outflows while some weak accretors may drive powerful outflows. For example, the outflow lines from GM Tau and 2M0414+2811 are substantially stronger than those from CIDA 1, despite the higher mass accretion rate onto CIDA 1. Similarly, many bright outflow lines are detected from 2M0444+2512 despite a modest mass accretion rate. The He I and Na I D lines are usually associated with both infall and outflow (Hartigan et al. 1995; Beristain et al. 2001; Edwards et al. 2006) but here are more tightly correlated with the accretion luminosity than [O I].

5.4. Comparison with \dot{M} measurements from emission line fluxes

In §5.3 we derive empirical relationships between line and accretion continuum luminosity. Lacking flux-calibrated spectra, Muzerolle et al. (1998) and Mohanty et al. (2005) converted the Ca II equivalent width into line flux per stellar surface area and then correlated the line flux directly with \dot{M} . Such a correlation naturally corrects for radius uncertainties introduced by errors in extinction or distance. Compared with equation 1, correlating $\frac{L_{line}}{R_*^2}$ with \dot{M} will be in error in \dot{M} by a factor of $\frac{M}{R_*^3}$.

Figure 11 compares the Ca II $\lambda 8542$, Ca II $\lambda 8662$, and He I $\lambda 5876$ line fluxes with accretion rate for the low-mass accretors presented here, high-mass accretors from Muzerolle et al. (1998 for the $\lambda 8542$), and low- and high-mass accretors from Mohanty et al. (2005 for the $\lambda 8662$ line)⁶. Those data have \dot{M} and Ca II line fluxes measured from non-contemporaneous observations and will suffer from variability. The $F(\text{Ca II } \lambda 8542) - \dot{M}$ and $F(\text{He I}$

$\lambda 5876) - \dot{M}$ relationships are shallower than was previously measured from only the high-mass sample, while the $F(\text{Ca II } \lambda 8662) - \dot{M}$ relationship is similar to that derived by Mohanty et al. (2005). The standard deviations between \dot{M} predicted from these line correlations and the \dot{M} measured from UV continuum excess are 1.0, 0.71, and 1.1 dex for Ca II $\lambda 8542$, Ca II $\lambda 8662$, and He I $\lambda 5876$ line fluxes, respectively.

6. DISCUSSION

6.1. Selecting methods to measure \dot{M}

In the magnetospheric accretion paradigm, the Paschen continuum emission is produced in optically-thick post-shock gas, the Balmer continuum emission is produced in optically-thin pre-shock gas, and the Balmer line emission is mostly produced primarily in the magnetospheric accretion column (Hartmann et al. 1994; Calvet & Gullbring 1998; Muzerolle et al. 2001; Kurosawa et al. 2006). In the simplistic plane-parallel models all three accretion diagnostics are produced by the same gas. In either case, the accretion energy is reprocessed into Balmer and Paschen continuum emission, which can be measured and subsequently converted into accretion rate. Previously, the accretion continuum measurements were applied only to accretors with $\sim 0.3 - 2 M_\odot$. Muzerolle et al. (2003) developed models to measure \dot{M} from H α line profiles for only the very low-mass stars and brown dwarfs. At higher mass accretion rates the H α emission line profile is difficult to use for estimating \dot{M} because emission and absorption in strong stellar outflows corrupt the line profile (Muzerolle et al. 2001; Kurosawa et al. 2006). We provide the first measurements of the Balmer continuum emission from very low-mass stars and brown dwarfs and describe this emission as qualitatively similar to that from higher-mass accretors. The UV excess measures of \dot{M} are $\sim 4 - 7$ times larger than those from H α line profile modelling with some source-to-source differences that may be methodological or related to intrinsic source variability.

In the context of magnetospheric accretion models, that the excess accretion continuum and the H α emission yield different \dot{M} may not be surprising because they form in different locations. The primary advantage of the H α models is that the line profile is independent of the intrinsic line luminosity and only moderately dependent on the stellar mass. According to Muzerolle et al. (2003), the uncertainty in \dot{M} from H α modelling is a factor of 3–5 and is dominated by uncertainty in the size of the magnetosphere. The factor of ~ 4 random error in UV excess measures of accretion is dominated by errors in extinction and distance. The UV excess method relies predominantly on directly observable parameters, with modelling required only for calculating a moderate bolometric correction to derive L_{acc} . The accretion energy is converted to \dot{M} by equation 1. In contrast, accretion

⁵ In Valenti et al. (1993) and here, the Balmer and Ca II H & K lines are measured directly from the spectrum while Gullbring et al. (1998) measures line fluxes after the subtraction of a photospheric template. These two different methods would slightly exacerbate the discrepancy between the line luminosities.

⁶ We calculate $\log \dot{M} = 1.28 \log F(\text{Ca II } \lambda 8542) - 16.6$, $\log \dot{M} =$

$1.03 \log F(\text{Ca II } \lambda 8662) - 15.2$, and $\log \dot{M} = 1.63 \log F(\text{He I } \lambda 5876) - 17.9$ from line fluxes and UV excess measures of accretion. We also note that the relative fluxes in the three Ca II IR triplet lines are usually consistent with the optically-thick limit of 1:1:1 (Herbig & Soderblom 1980; Hamann & Persson 1989), whether the emission is in a broad or narrow line (Batalha et al. 1996). Even at high-resolution all three Ca II IR triplet lines blend with Paschen lines.

rates from the H α line profile rely on a correct interpretation and modelling of the line profile in the magnetospheric funnel flow, and may be complicated by outflows, emission from hotspots, complex magnetic fields, or unexpected geometries.

Figures 12-13 compares the spectral properties of the excess hydrogen continuum emission versus stellar mass and mass accretion rate. The size of the Balmer jump tends to increase with decreasing M (and \dot{M}), consistent with lower n_e ($\sim 3 \times 10^{13} \text{ cm}^{-3}$ for 2M1207-3932 compared with $\sim 2 \times 10^{14} \text{ cm}^{-3}$ for higher mass accretors) in single-temperature slab models or with a larger contribution of emission from the optically-thin pre-shock gas relative to optically-thick post-shock gas in the magnetospheric accretion models. The slope of the Balmer continuum, which may be affected by our atmospheric correction, tends to increase with decreasing M (and \dot{M}). This is consistent with a lower temperature ($\sim 7500 \text{ K}$ for 2M1207-3932, compared with $\sim 8000 - 12000 \text{ K}$ for higher-mass accretors) in the plane-parallel slab models. Muzerolle et al. (2003) describes that the temperature in the magnetospheric accretion flow must be at least 10^4 K to have sufficient opacity in H α to produce the broad line profiles. The percent of the stellar surface subtended by the accretion hot spot (δ , see Table 11)⁷ is typically 0.01-1% for low-mass stars and brown dwarfs, relative to 0.1-10% for higher-mass stars (Valenti et al. 1993). These results should be fully accounted for as tests of the magnetospheric accretion models.

For regions with low extinction the UV excess method is the most accurate measure of accretion luminosity. The accretion luminosity can also be measured from the Paschen continuum at 3700–8000 Å, albeit with larger uncertainties and reduced sensitivity to small accretion rates. UV excess measures of accretion can be applied to even lower mass objects than studied here, limited only by telescopic sensitivity. H α line modelling may be a sufficient substitute for low-mass stars and brown dwarfs when UV excess measures are not possible, either due to large or uncertain extinction or distance, or instrumentation limitations. The H α models at present cannot be applied to large \dot{M} due to complex line profiles. They also cannot be applied to $\dot{M} < 10^{-12} M_{\odot} \text{ yr}^{-1}$, below which the opacity in the H α line wings may be insufficient to measure accretion (Muzerolle et al. 2003). However, H α models may be better suited than UV excess measurements for small \dot{M} onto higher mass/luminosity accretors, where the contrast between the Balmer continuum and photospheric emission is small. For example, the excess Balmer emission is difficult to detect onto the objects CIDA-14, V927 Tau, and 2M0455+3028, but the 10% width of the H α line is large enough to suggest accretion. Additional comparisons of \dot{M} between these two methods are required to better characterize the differences.

Secondary diagnostics, such as the Ca II IR triplet, Pa β , or Br γ lines, are related to L_{acc} or, less accurately, \dot{M} by empirical relationships and can provide useful

\dot{M} estimates (see also Muzerolle et al. 1998; Natta et al. 2004; Mohanty et al. 2005). The many random uncertainties inherent in both the UV excess and H α methods are reduced if the sample size is large enough. However, systematic uncertainties in the both accretion measures are propagated into these correlations. Some uncertainty is also introduced into these relationships because the line emission may be produced in different gas than the accretion continuum and because wind absorption can reduce the line flux. Of the line luminosity-accretion luminosity relationships analyzed in Table 15, the accretion luminosities estimated from the high Balmer lines and the He I $\lambda 5016$ line have the least amount scatter. The line luminosity-accretion luminosity relationships are preferable to line flux- \dot{M} relationships (Fig. 11), which have scatters of $\sim 0.75 - 1.0$ dex. That this amount of scatter is similar to the scatter in the $M - \dot{M}$ relationship (see §6.2) suggests that the line flux- \dot{M} relationships are not accurate.

Many of the commonly used lines (Ca II IR triplet, Pa β , Br γ) are less sensitive to \dot{M}/M than either the H α line profile or excess UV emission. They therefore provide a less complete picture of the full range of accretion. The completeness depends on mass if detection limit of each diagnostic varies with spectral type. These diagnostics are often more accessible than modelling H α profiles or measuring the UV excess and are particularly useful for variability studies of a individual objects (e.g. Alencar et al. 2005; Azevedo et al. 2006) or in large samples (Natta et al. 2006).

6.2. Accretion rate versus mass

Figure 14 shows \dot{M} versus M for Taurus accretors with $A_V < 2.5$ from Gullbring et al. (1998), Hartigan & Kenyon (2003), Calvet et al. (2004), Muzerolle et al. (2005), and from the low-resolution *Keck I* and *HST* spectra analyzed in this work⁸. We use *asurv* (Feigelson & Nelson 1985) to calculate that

$$\log \dot{M} = (1.87 \pm 0.26) \log M - (7.73 \pm 0.17), \quad (2)$$

which is similar to previous estimates of $\dot{M} \propto M^{1.8-2.3}$ (Muzerolle et al. 2005; Mohanty et al. 2005; Natta et al. 2006). The standard deviation of the fit to \dot{M} is 0.8 dex. This standard deviation is too large to be explained by intrinsic accretion variability or random methodological uncertainties, which suggests that stellar parameters other than mass also affect the accretion rate. A lack of completeness in our sampling of the true range in mass accretion rate for a given mass can bias the $\dot{M} - M^{\alpha}$ relationship by target selection and by sensitivity limits.

We specifically selected several targets (CIDA 1, GM Tau, and 2M0414+2811) based on our expectation of high \dot{M} . Most other stars were selected based in part on visual magnitude, which may tend to yield sources with higher \dot{M} . If this selection bias is only present in the current data, which focuses on the low-mass range, then the α in the $\dot{M} - M^{\alpha}$ relationship will be underestimated. However, a similar bias could also be present in

⁷ The estimates of δ are inversely correlated with L , the length of the accretion slab, and T , the temperature of the accretion slab. The calculated L may be non-physical, and in this work are larger here than the $\sim 10^7$ typical for Valenti et al. (1993). As a result, the difference in δ between the two works may be underestimated.

⁸ The Hartigan & Kenyon (2003) data are used to re-calculate accretion rates, as in §5.1. The Muzerolle et al. (2005) accretion rates are used only if they are not duplicates from this work and are multiplied by a factor of 5 (see §5.3). Duplicate measurements of \dot{M} for the same star are averaged.

previous \dot{M} measurements from samples of higher-mass stars.

The \dot{M} from higher-mass accretors may be incomplete because sensitivity to $\frac{\dot{M}}{M}$ improves to smaller masses for both UV excess and H α accretion measures. Figure 15 shows that accretion luminosity and the measured $\frac{L_{acc}}{L_{bol}}$ decreases with mass. The improved sensitivity to low $\frac{L_{acc}}{L_{bol}}$ at smaller masses results because the percentage of total photospheric emission that escapes at $< 3700 \text{ \AA}$ is much less for mid-late M-dwarfs than for late-K dwarfs. In Valenti et al. (1993) and Gullbring et al. (1998), the minimum value of $\frac{L_{acc}}{L_{bol}}$ is 0.008 and 0.018, respectively, with most targets well above that limit. This detection limit leads to $\dot{M} \sim 5 - 10 \times 10^{-10} M_{\odot} \text{ yr}^{-1}$ for a 2 Myr old $0.7 M_{\odot}$ star with $L = 0.57 L_{\odot}$. For the lower-mass accretors studied here, accretion from 2M0455+3028 is at our detection limit with $\frac{L_{acc}}{L_{phot}} \sim 0.001$. For a 2 Myr old, $0.1 M_{\odot}$ brown dwarf, the lowest detectable mass accretion rate is $\sim 10^{-11} M_{\odot} \text{ yr}^{-1}$. The $\frac{\dot{M}}{M}$ ratio is therefore about 5.5 times lower for a $0.1 M_{\odot}$ accretor than for a $0.7 M_{\odot}$ accretor. Incompleteness at higher masses would cause us to overestimate α in the $\dot{M} - M^{\alpha}$ relationship. On the other hand, inclusion of the five tentative accretors would increase α to 2.08.

7. CONCLUSIONS

We analyzed blue spectra of 18 accreting very low-mass stars and brown dwarfs obtained with LRIS on *Keck I*. Ours are the first data on the Balmer continuum and high Balmer line emission in this mass range. Most of this sample was selected based on the presence of accretion identified with other diagnostics. Our observations are compared with archival *HST*/STIS spectra of the Balmer continuum from several higher-mass stellar accretors. We obtain the following results:

1. We detect excess hydrogen Balmer continuum emission from 16 of the 18 mid-late M-dwarfs in our sample. 11 of these objects also show hydrogen Paschen continuum emission. This continuum is attributed to accretion for most of our objects. Weak Balmer continuum emission onto earlier-type stars, including the K6 dwarf V836 Tau, can be attributed to accretion because non-accretors show no evidence for chromospheric Balmer continuum emission. However, we cannot rule out a chromospheric origin for weak excess Balmer emission from mid-M dwarfs.

2. Measurements of the Balmer and Paschen continua emission yield $\dot{M} = 10^{-12} - 10^{-8}$ for very-low mass stars and brown dwarfs with masses from $0.024 - 0.17 M_{\odot}$. Most of these accretion rates are smaller than those typically measured for accreting $\sim 0.3 - 1.0 M_{\odot}$ stars. Analysis of the random and systematic errors indicate that these \dot{M} may be underestimated by a factor of 1.2 (or 2.4 if the hydrogen continuum emission incident upon the star is reprocessed into photospheric emission), with a relative uncertainty of ~ 0.6 dex. Comparing these \dot{M} with \dot{M} from other studies requires accounting for different assumptions regarding radiative transfer.

3. The Balmer jump tends to be larger and the Balmer continuum tends to be redder for stars with lower mass accretion rates. These properties indicate lower opacity (with $\log n_e = 13.5$ for 2M1207, compared with $\log n_e \sim$

- 14.3 for stars with higher \dot{M} in the plane-parallel slab models) and lower temperature (with $T \sim 7000 \text{ K}$ for 2M1207, compared with ~ 9500 for stars with higher \dot{M}).

4. The \dot{M} calculated here are well correlated with but $\sim 4 - 7$ times larger than the \dot{M} calculated from published models of the H α line profiles. We suggest that this offset is methodological, although the difference is within the range of the combined errors for both methods. The \dot{M} measured here also correlates with H α 10% width but introduces 0.9 dex uncertainty in \dot{M} predicted from H α 10% width alone.

5. We provide empirical relationships between L_{acc} and L_{line} , which are often well correlated. In particular, estimating L_{acc} from the luminosity in the high Balmer and many He I lines introduces an uncertainty of only 0.2–0.35 dex. On the other hand, estimating the L_{acc} from line surface fluxes alone introduces an uncertainty of $\sim 0.7 - 1.1$ dex in \dot{M} estimates.

6. We find that $\log \dot{M} \propto M^{1.87}$ for Taurus stars with $A_V < 2.5$, which is consistent with previous estimates. This relationship may be biased if the higher sensitivity of \dot{M}/M at lower M causes the percentage of accretors that are detected to also vary with M .

8. ACKNOWLEDGEMENTS

We thank Jeff Valenti and Chris Johns-Krull for use of their plane-parallel slab model codes that they developed in Valenti et al. (1993). We thank Russel White for discussion of the proposal and Nuria Calvet for discussion of the line emission. We thank the anonymous referee for helpful comments, which served to improve the structure and clarity of the paper.

Most of data presented herein were obtained at the W.M. Keck Observatory, which is operated as a scientific partnership among the California Institute of Technology, the University of California and the National Aeronautics and Space Administration. The Observatory was made possible by the generous financial support of the W.M. Keck Foundation. Some of the data presented in this paper were obtained from the Multimission Archive at the Space Telescope Science Institute (MAST). STScI is operated by the Association of Universities for Research in Astronomy, Inc., under NASA contract NAS5-26555. Support for MAST for non-HST data is provided by the NASA Office of Space Science via grant NAG5-7584 and by other grants and contracts.

9. APPENDIX

9.1. Photospheric Emission

The photospheric emission from M-dwarfs is dominated by strong TiO and CaH bands at $\lambda > 4800 \text{ \AA}$ that can be used to estimate spectral type (e.g. Kirkpatrick et al. 1993). Table 3 lists spectral types for our targets estimated from the TiO 7140 and 8465 \AA indices (Slesnick et al. 2006) and by visual comparison to existing *Keck I*/LRIS spectra of M4.5-M9.5 M-dwarfs⁹. Most spectral types are consistent with existing literature estimates. We classify V927 Tau as an M5 star, compared with previous classifications of M3, M4.75, and M5.5. 2M0455+3028, S0439+2336, and MHO 6 have the same spectral type as V927 Tau and are classified as M5. MHO 7 is a slightly later spectral type

than V927 Tau and is classified as M5.5, 0.25 classes later than in Briceno et al. (2002). The photospheric emission from CIDA 14 is nearly identical to MHO 7. S0518+2327 is about the same as MHO 7 and classified as M5.5, while KPNO Tau 11 slightly later than MHO 7 and is classified as an M5.75. MHO 5 is between MHO 7 and CFHT 7 and is classified as M6. We confirm spectral types from Luhman (2004) for 2M0438+2611, 2M0439+2544, 2M0441+2534, and 2M0444+2512, and from Gizis (2002) for 2M1207-3932. We conservatively assign a 0.5 subclass uncertainty to all spectral types.

The spectral types for GM Tau, CIDA 1, and 2M0414+2811 are difficult to determine because of high veiling at $\lambda > 7000$ Å. In order to make some estimate we assume that the accretion continuum emission is constant in flux per Å across short wavelength intervals. The depth of absorption bands are then compared to spectral type standards to estimate the spectral classification. The photospheric emission of CIDA 1 is consistent with M5, GM Tau with M5.5, and 2M0414+2811 with CFHT 7. The spectral types of CIDA 1 and GM Tau are 0.5 and 1 class earlier, respectively, than that measured by White & Basri (2003) and are both assigned an error of 1.0 subclasses.

9.2. Extinction

Extinction estimates are important to convert the measured flux in the accretion continuum into a luminosity. Many of our targets were selected for observation based on low extinction. We adopt extinctions of ~ 0.4 , 0.1, 0.0, and 0.0 to the non-accretors V927 Tau, MHO 7, CFHT 7, and the accretors 2M0444+2512 (Kenyon & Hartmann 1995; Briceno et al. 2002; Guieu et al. 2007; Luhman 2004). We confirm these estimates with an accuracy of ~ 1.0 mag by comparing our flux-calibrated observations to existing *Keck I*/LRIS red spectra (6000–10000 Å) of photospheric templates.

The photospheric emission from the rest of our targets are then compared to those four templates to calculate an extinction. For accretors, we also add a flat accretion continuum at red wavelengths. We use the extinction law from Cardelli et al. (1989) and a total-to-selective extinction (R_V) of 3.1. Some evidence suggests that $R_V > 3.1$ in the Taurus Molecular Cloud because grains in the molecular cloud may be larger than those in the average interstellar medium (Whittet et al. 2001). If R_V is large, the slope of extinction versus wavelength is shallow and A_V will be underestimated. The spectrum of 2M0438+2611 is likely seen through an edge-on disk and suffers from gray extinction and scattering (Luhman et al. 2007) that is not corrected for here.

We confirm our extinction estimates for sources with strong veiling by assuming that the Paschen continuum between 4000–6000 Å is flat (see §3.1), which is roughly consistent with observations of the higher-mass accretors (e.g. Basri & Batalha 1990; Hartigan et al. 1991), with observations of accretors with low A_V (Gullbring et al. 2000), and with shock models (Calvet & Gullbring 1998).

Our extinction estimates are listed in Table 3. Any

error in the A_V for V927 Tau, MHO 7, CFHT 7, and 2M0444+2512 will propagate to the remaining data. Our estimates are consistent with previous extinction estimates (Briceno et al. 2002; Luhman 2004), with a few exceptions. We estimate $A_V \sim 1.0$ and ~ 0.7 to 2M0455+3028 and 2M0439+2544, respectively, compared with $A_J = 0.0$ and 0.07 from Luhman (2004). We measure $A_V = 2.0 \pm 0.7$ to GM Tau, less than previous estimates of ~ 4.2 mag (Briceno et al. 2002; Guieu et al. 2007).

2M1207-3932 is in the TW Hya Association and isolated from molecular gas. We assume $A_V = 0$ to 2M1207-3932, and confirm that $A_V < 1$ by comparison to a template LRIS M8-dwarf standard.

9.3. Stellar Radius and Mass

Estimates for the stellar mass and radius are required to calculate mass accretion rates. The spectral class is converted to temperature using the scale derived by Luhman et al. (2003). We then use our spectral types, extinction estimates, synthetic R-band photometry (after correcting for the measured veiling), and Baraffe et al. (1998) evolutionary tracks to compute the stellar luminosity, mass, radius, and age (see Table 3). The calculated ages for the higher-mass sample in Taurus are overestimated, which is consistent with known systematic problems in stellar evolutionary tracks (Hillenbrand et al. 2007)

A distance of 140 pc is assumed for Taurus stars (Kenyon et al. 1994). Slesnick et al. (2006) identified S0518+2327 as an accretor away from the main Taurus molecular cloud and classify it as an intermediate-age star based on the depth of Na I gravity indices. The distance to S0518+2327 is therefore more uncertain than the most other Taurus stars. We adopt a parallax distance of 54 ± 3 pc to 2M1207-3932 (Gizis et al. 2007; see also Biller & Close 2007) and of 56 pc for TW Hya (Wichmann et al. 1998).

Any binarity in our sample would reduce the stellar luminosity and estimated radius. Kraus et al. (2006) found that GM Tau and MHO 5 are spatially unresolved to $\sim 0''.05$ and are either single stars or spectroscopic binaries. We assume our other targets are single stars with the exception of V927 Tau (see §9.4.2).

9.4. Notes on Individual Objects

9.4.1. 2M1207-3932

2M1207-3932 is a M8-L dwarf binary (Gizis 2002; Chauvin et al. 2004) in the 10 Myr old TW Hya Association (Webb et al. 1999; Mamajek 2005). The primary has an IR excess and ongoing accretion. The secondary is faint and undetected in our data. We observed 2M1207-3932 on both November 24 and February 8. The February observation was deeper and obtained with the target at lower airmass. The flux from the November integration is calibrated based on the strength of photospheric emission from 6000–8000 Å measured in the February run. The blue and UV continuum emission was fainter in November than on February 8. Most of these parameters have a higher confidence for 2M1207-3932 than the Taurus members.

Stelzer et al. (2007) applied the Natta et al. (2004) relationship for H α 10% width to measure $\dot{M} \sim 10^{-10.1} -$

⁹ Obtained from <http://www-int.stsci.edu/~inr/ultracool.html> (Gizis et al. 2000ab, Kirkpatrick et al. 1999).

$10^{-9.8} M_{\odot} \text{ yr}^{-1}$ from 2M1207-3932, which is two orders of magnitude larger than measured here. This difference is not likely attributed to variability because the $\text{H}\alpha$ equivalent width during our February observation is the largest yet detected from 2M1207-3932. During an epoch in 2003 with low \dot{M} (Stelzer et al. 2007), both the equivalent width and $\text{H}\alpha$ 10% width were small. The variable equivalent width in the $\text{Ca II } \lambda 8542$ line of $< 0.3 \text{ \AA}$ (Stelzer et al. 2007) corresponds to $\dot{M} < 2.1 \times 10^{-12} M_{\odot} \text{ yr}^{-1}$ (Table 15), which confirms our low \dot{M} .

9.4.2. V927 Tau

V927 Tau is a binary separated by $\sim 0''.27$ (Leinert et al. 1993; White & Ghez 2001). Muzerolle et al. (2003) measured a broad 10% width of 290 km s^{-1} and only a small self-reversal in the symmetric $\text{H}\alpha$ line profile from V927 Tau. They suggested that this $\text{H}\alpha$ emission may be produced by chromospheric flaring since most $\text{H}\alpha$ profiles produced by accretion are asymmetric. At the time no excess IR or sub-mm emission had been detected from either component (Simon & Prato 1995; White & Ghez 2001; Andrews & Williams 2005). However, McCabe et al. (2006) measured K-band magnitudes that were the same as measured by White & Ghez (2001), but L-band emission that was brighter by 1 magnitude for both V927A and B. Such variability may suggest that the amount of warm dust in the disk is variable, and that perhaps accretion onto V927 Tau may sometimes be present.

We detect some excess Balmer continuum and He I $\lambda 5876$ emission from V927 Tau relative to MHO 7. V927 Tau and its template MHO 7 are slightly different spectral types, which may lead to some discrepancy in this comparison. Such emission could be interpreted as either chromospheric or accretion-related. Hartigan & Kenyon (2003) found weak excess Paschen continuum emission from the secondary, if the secondary is classified as an M3.5 star. V927 Tau remains ambiguous as to whether accretion is ongoing.

9.4.3. 2M0438+2611

We obtain a short LRIS spectrum of 2M0438+2611, which Luhman et al. (2007) describe as a young accreting star seen through an edge-on disk with a gray extinction of 5.5 mag. The gray extinction cannot be measured from the shape of the continuum emission, which is similar to that of 2M0444+2512 ($A_V = 0$ mag). If we assume the two stars have the same radius, then we find $A_V = 2.8$ mag to 2M0438+2611. That the optical forbidden lines are bright (see also Luhman 2004; Luhman et al. 2007) indicates that some of the outflow emission is at least slightly extended and not absorbed by the edge-on disk, consistent with other accretors seen through edge on disks.

We classify 2M0438+2611 as a moderate accretor based on the detection of optical forbidden lines and non-detection of the Ca II IR triplet. We use the $\text{H}\gamma$ line luminosity and Table 12 to calculate $L_{acc} \sim 4 \times 10^{-5} L_{\odot}$, or $\dot{M} \sim 1.5 \times 10^{-11} M_{\odot} \text{ yr}^{-1}$ (assuming same M and R are the same as 2M0444+2512). The upper limit for the $\text{Ca II } \lambda 8542$ equivalent width of $< 1.2 \text{ \AA}$ indicates $L_{acc} < 1.6 \times 10^{-4} L_{acc}$. We do not use the \dot{M} of

2M0438+2611 in any analysis.

9.4.4. 2M0414+2811

2M0414+2811 is about a magnitude brighter and is bluer than UBV photometry obtained by Grosso et al. (2007), which suggests a higher \dot{M} during our observation.

9.4.5. MHO 5

Emission in the $[\text{O I}] \lambda 6300, 6363$ and He I $\lambda 5876$ lines are detected with equivalent width typical of accretors. MHO 5 is therefore classified as an accretor, despite a low $\text{H}\alpha$ 10% width of 154 km s^{-1} (Muzerolle et al. 2003). Ongoing accretion indicates that the weak excess Balmer continuum emission is likely produced by accretion, although we cannot rule out a chromospheric origin.

9.4.6. CIDA 14

The excess Balmer continuum emission onto CIDA 14 is very weak, and only detected because the photospheric emission is very similar to that from the non-accretor MHO 7. We detect an equivalent width of 0.27 \AA in the $[\text{O I}]$ line from CIDA 14, which is slightly lower than the 0.4 \AA measured by Briceno et al. (1999) but larger than the $< 0.1 \text{ \AA}$ upper limit from high-resolution spectra by Muzerolle et al. (2003). This low upper limit may be underestimated if the line is broad. Muzerolle et al. (2003) measured an $\text{H}\alpha$ equivalent width of 289 km s^{-1} . CIDA 14 is a likely accretor.

9.4.7. KPNO 11

Several He I lines that are undetected from the non-accretors are detected from KPNO 11 (Table 5). However, the strength of the He I $\lambda 5876 \text{ \AA}$ line and the upper limit on the Na I D line luminosity are below the expected luminosity for the calculated \dot{M} . These luminosities may suggest that the excess Balmer continuum emission and He I lines are chromospheric. The $\text{H}\alpha$ 10% width of 182 km s^{-1} (Mohanty et al. 2005) is intermediate between accretors and non-accretors.

9.4.8. GM Tau

The flux ratio of Balmer line emission to Balmer continuum emission from GM Tau is much smaller than measured for any other source here, which requires a large optical depth in the slab.

9.4.9. S0518+2327

S0518+2327 is an accretor located away from the main Taurus Molecular Cloud (Slesnick et al. 2006). The distance to this star is more uncertain than the other Taurus stars studied here.

9.4.10. 2M0436+2351

The U-band atmospheric correction for 2M0436+2351 is somewhat uncertain. As a result, no slope for the Balmer continuum is listed in Table 5. The mass accretion rate for this star is also more uncertain than that of other stars in our sample.

9.4.11. *DF Tau*

DF Tau is a 0'1 binary (Schaefer et al. 2006) that is unresolved in these spectra. When calculating the stellar radius we assumed that the luminosity of the two stars are equal. STIS observed DF Tau three times with the G430L grating, two of which are analyzed here. The third observations shows much weaker photospheric and continuum emission with an accretion rate 10 times lower than the other observations (Herczeg et al. 2006). We do not analyze this third spectrum here because it was obtained with a narrower slit and could have included

the secondary but not the primary.

9.4.12. *DG Tau*

We measure $\dot{M} = 4.1 \times 10^{-9} M_{\odot} \text{ yr}^{-1}$, an order of magnitude less than that measured by Gullbring et al. (2000). The spectrum of DG Tau during the Gullbring et al. (2000) observation was heavily-veiled and an order of magnitude brighter than that detected here. The different \dot{M} result from real variability. Strong emission is detected in forbidden lines and Fe I lines despite the lower \dot{M} .

REFERENCES

- Alencar, S.H.P., Basri, G., Hartmann, L., & Calvet, N. 2005, *A&A*, 440, 595
- Allred, J.C., Hawley, S.L., Abbett, W.P., & Carlsson, M. 2006, *ApJ*, 644, 484
- Andrews, S.M., & Williams, J.P. 2005, *ApJ*, 631, 1134
- Azevedo, R., Calvet, N., Hartmann, L., Folha, D.F.M., Gameiro, F., & Muzerolle, J. 2006, *A&A*, 456, 225
- Baraffe, I., Chabrier, G., Allard, F., & Hauschildt, P.H. 1998, *A&A*, 337, 403
- Basri, G., & Batalha, C. 1990, *ApJ*, 363, 654
- Batalha, C.C., Stout-Batalha, N.M., Basri, G., & Terra, M.A.O. 1996, *ApJS*, 103, 211
- Batalha, C., Batalha, N.M., Alencar, S.H.P., Lopes, D.F., & Duarte, E.S. 2002, *ApJ*, 580, 343
- Beristain, G., Edwards, S., & Kwan, J. 2001, *ApJ*, 551, 1037
- Bertout, C., & Genova, F. 2006, *A&A*, 460, 499
- Biller, B.A., & Close, L.M. 2007, *ApJ*, 669, L41
- Bohlin, R.C., Savage, B.D., & Drake, J.F. 1978, *ApJ*, 224, 132
- Bouvier, J., Alencar, S.H.P., Boutelier, T., Dougados, C., Balog, Z., Grankin, K., Hodgkin, S.T., Ibrahimov, M.A., Kin, M., Magakian, T. Yu., Pinte, C. 2007, *A&A*, 463, 1017
- Briceno, C., Calvet, N., Gomez, M., Hartmann, L.W., Kenyon, S.J., & Whitney, B.A. 1993, *PASP*, 105, 686
- Briceno, C., Hartmann, L., Stauffer, J., & Martin, E. 1998, *ApJ*, 115, 2074
- Briceno, C., Calvet, N., Kenyon, S., & Hartmann, L. 1999, *ApJ*, 118, 1354
- Briceno, C., Luhman, K.L., Hartmann, L., Stauffer, J.R., & Kirkpatrick, J.D. 2002, *ApJ*, 580, 317
- Calvet, N., & Gullbring, E. 1998, *ApJ*, 509, 802
- Calvet, N., Muzerolle, J., Briceno, C., Hernandez, J., Hartmann, L., Saucedo, J.L., & Gordon, K.D. 2004, *AJ*, 128, 1294
- Cardelli, J. A., Clayton, G. C., & Mathis, J. S. 1989, *ApJ*, 345, 245
- Cardini, D., & Cassatella, A. 2007, *ApJ*, 666, 393
- Carpenter, J.M., Mamajek, E.E., Hillenbrand, L.A., & Meyer, M.R. 2006, *ApJ*, 651, L49
- Chauvin, G., Lagrange, A.-M., Dumas, C., Zuckerman, B., Mouillet, D., Song, I., Beuzit, J.-L., Lowrance, P. 2004, *A&A*, 425, L29
- Cieza, L.A., Kessler-Silacci, J.E., Jaffe, D.T., Harvey, P.M., & Evans, N.J. 2005, *ApJ*, 635, 422
- Clarke, C.J., & Pringle, J.E. 2006, *MNRAS*, 370, L10
- D'Antona, F., & Mazzitelli, I. 1998, *ASPC*, 134, 442
- Eason, E. L. E., Giampapa, M. S., Radick, R. R., Worden, S. P., & Hege, E. K. 1992, *AJ*, 104, 1161
- Edwards, S., Fischer, W., Hillenbrand, L.A., & Kwan, J. 2006, *ApJ*, 646, 319
- Feigelson, E.D., & Kriss, G.A. 1981, *ApJ*, 248, L35
- Feigelson, E.D., & Nelson, P.I. 1985, *ApJ*, 293, 192
- Giampapa, M.S., Worden, S.P., & Linsky, J.L. 1982, *ApJ*, 258, 740
- Gizis, J.E., Monet, D.G., Reid, I.N., Kirkpatrick, J.D., Liebert, J., Williams, R. 2000, *AJ*, 120, 1085
- Gizis, J.E., Monet, D.G., Reid, I.N., Kirkpatrick, J.D., Burgasser, A.J. 2000, *MNRAS*, 311, 385
- Gizis, J.E. 2002, *ApJ*, 575, 484
- Gizis, J.E., Reid, I.N., & Hawley, S.L. 2002, *AJ*, 123, 3356
- Gizis, J.E., Jao, W.-C., Subasavage, J.P., & Henry, T.J. 2007, *ApJ*, 669, L45
- Grosso, N., et al. 2007, *A&A*, 468, 391
- Guieu, S., Dougados, C., Monin, J.-L., Magnier, E., & Martin, E.L. 2006, *A&A*, 446, 485
- Guieu, S., et al. 2007, *A&A*, 465, 855
- Gullbring, E., Hartmann, L., Briceno, C., & Calvet, N. 1998, *ApJ*, 492, 323
- Gullbring, E., Calvet, N., Muzerolle, J., & Hartmann, L. 2000, *ApJ*, 544, 927
- Hamann, F., & Persson, S. E. 1989, *ApJ*, 339, 1078
- Hamann, F., & Persson, S. E. 1992, *ApJS*, 82, 247
- Hamann, F. 1994, *ApJS*, 93, 485
- Hartigan, P., Kenyon, S.J., Hartmann, L., Strom, S.E., Edwards, S., Welty, A.D., & Stauffer, J. 1991, *ApJ*, 382, 617
- Hartigan, P., Edwards, S., & Ghandour, L. 1995, 452, 736
- Hartigan, P., & Kenyon, S.J. 2003, *ApJ*, 583, 334
- Hartigan, P., Edwards, S., & Pierson, R. 2004, *ApJ*, 609, 261
- Hartmann, L., Hewett, R., & Calvet, N. 1994, *ApJ*, 426, 669
- Hawley, S. L., & Pettersen, B. R. 1991, *ApJ*, 378, 725
- Henize, K.G. 1954, *ApJ*, 119, 459
- Herbig, G.H., & Kameswara, R.N. 1972, *ApJ*, 174, 401
- Herbig, G.H., & Soderblom, D.R. 1980, *ApJ*, 242, 628
- Herbig, G.H., Vrba, F.J., & Rydgren, A.E. 1986, *AJ*, 91, 575
- Herczeg, G.J., Wood, B.E., Linsky, J.L., Valenti, J.A., Johns-Krull, C.M. 2004, *ApJ*, 607, 369
- Herczeg, G.J., et al. 2005, *ApJ*, 129, 2777
- Herczeg, G.J., Linsky, J.L., Walter, F.M., Gahm, G.F., & Johns-Krull, C.M. 2006, *ApJS*, 165, 256
- Hillenbrand, L.A., Bauermeister, A., & White, R.J. 2007, *proc. of Cool Stars, Stellar Systems, and the Sun XIX*, APS Conference Series, eds. G. van Belle.
- Jayawardhana, R., Mohanty, S., & Basri, G. 2003, *ApJ*, 592, 282
- Johns-Krull, C.M., & Basri, G. 1997, *ApJ*, 474, 433
- Johns-Krull, C. M., Valenti, J. A., & Linsky, J. L. 2000, *ApJ*, 539, 815
- Johns-Krull, C.M. 2007, *ApJ*, 664, 975
- Kastner, J.H., Huenemoerder, D.P., Schulz, N.S., Canizares, C.R., & Weintraub, D.A. 2002, *ApJ*, 567, 434
- Kenyon, S.J., Dobrzycka, D., & Hartmann, L.W. 1994, *AJ*, 108, 1872
- Kenyon, S.J., & Hartmann, L. 1995, *ApJS*, 101, 117
- Kirkpatrick, J.D., Kelly, D.M., Rieke, G.H., Liebert, J., Allard, F., & Wehrse, Rainer. 1993, *ApJ*, 402, 643
- Kirkpatrick, J.D., et al. 1999, *ApJ*, 519, 802
- Kraus, A.L., White, R.J., & Hillenbrand, L.A. 2006, *ApJ*, 649, 306
- Kurosawa, R., Harries, T.J., & Symington, N.H. 2006, *MNRAS*, 370, 580
- Leinert, C., Zinnecker, H., Weitzel, N., Christou, J., Ridgway, S.T., Jameson, R., Haas, M., Lenzen, R. 1993, *A&A*, 278, L129
- Luhman, K.L., Stauffer, J.R., Muench, A.A., Rieke, G.H., Lada, E.A., Bouvier, J., & Lada, C.J. 2003, *ApJ*, 593, 1093
- Luhman, K.L. 2004, *ApJ*, 617, 1216
- Luhman, K.L., et al. 2006, *ApJ*, 647, 1180
- Luhman, K.L., Adame, L., D'Alessio, P., Calvet, N., McLeod, K.K., Bohac, C.J., Forrest, W.J., Hartmann, L., Sargent, B., & Watson, D.M. 2007, *ApJ*, 666, L1219
- Mamajek, E.E. 2005, *ApJ*, 634, 1385
- Massey, P., Strobel, K., Barnes, J.V., & Anderson, E. 1988, *ApJ*, 328, 315
- Mauas, P.J.D., & Falchi, A. 1996, *A&A*, 310, 245
- McCabe, C., Ghez, A.M., Prato, L., Duchene, G., Fisher, R.S., & Telesco, C. 2006, *ApJ*, 636, 932
- McCarthy, J. K., Cohen, J. G., Butcher, B., Cromer, J., Croner, E., Douglas, W. R., Goeden, R. M., Grewal, T., Lu, B., Petrie, H. L., Weng, T., Weber, B., Koch, D. G., & Rodgers, J. M. 1998, *SPIE*, 3355, 81
- Mohanty, S., Jayawardhana, R., & Basri, G. 2005, *ApJ*, 626, 498

- Muzerolle, J., Hartmann, L., & Calvet, N. 1998, *AJ*, 116, 2965
- Muzerolle, J., Calvet, N., Briceno, C., Hartmann, L., & Hillenbrand, L. 2000, *ApJ*, 535, L47
- Muzerolle, J., Calvet, N., & Hartmann, L. 2001, *ApJ*, 550, 944
- Muzerolle, J., Hillenbrand, L., Calvet, N., Briceno, C., & Hartmann, L. 2003, *ApJ*, 592, 266
- Muzerolle, J., Luhman, K.L., Briceno, C., Hartmann, L., & Calvet, N. 2005, *ApJ*, 625, 906
- Natta, A., Testi, L., Muzerolle, J., Randich, S., Comeron, F., & Persi, P. 2004, *A&A*, 424, 603
- Natta, A., Testi, L., & Randich, S. 2006, *A&A*, 452, 245
- Oke, J.B. 1990, *AJ*, 99, 1621
- Oke, J.B., Cohen, J.G., Carr, M., Cromer, J., Dingizian, A. & Harris, F. H. 1995, *PASP*, 107, 3750
- Rauscher, E., & Marcy, G.W. 2006, *PASP*, 118, 617
- Reipurth, B., Pedrosa, A., & Lago, M.T.V.T. 1996, *A&AS*, 120, 229
- Rucinski, S.M., & Krautter, J. 1983, *A&A*, 121, 217
- Rydgren, A.E., & Vrba, F.J. 1983, *AJ*, 88, 1017
- Schaefer, G.H., Simon, M., Beck, T.L., Nelan, E., & Prato, L. 2006, *ApJ*, 132, 2618
- Scholz, A., Jayawardhana, R., & Brandeker, A. 2005, *ApJ*, 629, L41
- Scholz, A., & Jayawardhana, R. 2006, *ApJ*, 638, 1056
- Short, C.I., Doyle, J.G., & Byrne, P.B. 1997, *A&A*, 324, 196
- Simon, M., & Prato, L. 1995, *ApJ*, 450, 824
- Slesnick, C.L., Carpenter, J.M., Hillenbrand, L.A., & Mamajek, E.E. 2006, *ApJ*, 132, 2665
- Smak, J. 1964, *ApJ*, 139, 1095
- Stelzer, B., Scholz, A., & Jayawardhana, R. 2007, *astro-ph*:/0707.1754
- Valenti, J.A., Basri, G., & Johns, C.M. 1993, *ApJ*, 106, 2024
- Valenti, J.A., Fallon, A.A., & Johns-Krull, C.M. 2003, *ApJS*, 147, 305
- Walter, F.M., & Kuhl, L.V. 1981, *ApJ*, 250, 254
- Webb, R.A., Zuckerman, B., Platais, I., Patience, J., White, R.J., Schwartz, M.J., McCarthy, C. 1999, *ApJ*, 512, L63
- Whelan, E.T., Ray, T.P., Randich, S., Bacciotti, F., Jayawardhana, R., Testi, L., Natta, A., & Mohanty, S. 2007, *ApJ*, 659, L45
- White, R.J., & Ghez, A.M. 2001, *ApJ*, 556, 265
- White, R.J., & Basri, G. 2003, *ApJ*, 582, 1109
- White, R.J., & Hillenbrand, L.A. 2004, *ApJ*, 616, 998
- Whittet, D.C.B., Gerakines, P.A., Hough, J.H., Shenoy, S.S. 2001, *ApJ*, 547, 872
- Wichmann, R., Bastian, U., Krautter, J., Jankovics, I., & Rucinski, S.M. 1998, *MNRAS*, 301, L39
- Yang, H., Johns-Krull, C.M., & Valenti, J.A. 2007, *AJ*, 133, 73

TABLE 1
 OBSERVATIONS WITH *Keck I*/LRIS

Star	MJD ^a	t_{exp}	U ^b	B ^b	V ^b	R ^b	σ^c (mag)	Abbreviation ^d
CIDA 1	63.318	720	18.6	18.3	17.2	15.3	0.6	CIDA 1
2MASS J04141188+2811535	63.329	1200	18.2	18.2	17.6	16.4	0.6	2M0414+2811
MHO-Tau 5	63.382	1620	19.2	18.3	16.9	15.0	0.4	MHO 5
MHO-Tau 6	63.405	1260	18.5	17.8	16.6	15.1	0.4	MHO 6
GM Tau	63.422	1050	18.7	18.7	17.8	16.3	0.4	GM Tau
2MASS J04390396+2544264	63.438	2700	22.0	21.5	20.1	17.6	0.4	2M0439+2544
2MASS J04442713+2512164	63.475	2100	21.0	20.4	19.5	17.3	0.4	2M0444+2512
CIDA 14	63.498	720	18.5	17.4	15.9	14.4	0.4	CIDA 14
SCH J0439016+2336030	63.508	840	18.1	17.2	15.9	14.6	0.3	S0439+2336
V927 Tau	63.520	150	17.3	16.1	14.8	13.3	0.3	V927 Tau
CFHT Tau 7	63.525	600	20.8	20.0	18.4	16.3	0.2	CFHT 7
MHO-Tau 7	63.532	600	19.1	18.0	16.6	15.0	0.2	MHO 7
2MASS J04381486+2611399	63.540	300	-	-	-	20.1	0.2	2M0438+2611
KPNO-Tau 11	63.552	900	20.1	19.1	17.7	15.9	0.2	KPNO 11
2MASS J04414825+2534304	63.567	2400	22.0	21.9	21.1	19.1	0.2	2M0441+2534
2MASS J04554757+3028077	63.600	1080	19.0	17.9	16.5	14.9	0.2	2M0455+3028
SCH J0518028+2327126	63.611	1380	18.3	18.2	17.8	16.6	0.2	S0518+2327
2MASS J12073347-3932540 ^e	63.647	840	21.1	21.3	20.5	18.2	0.2	2M1207-3932
2MASS J04362151+2351165	139.218	400	20.0	19.5	18.4	16.9	1.0	2M0436+2351
2MASS J12073347-3932540	139.611	1800	20.8	20.9	20.2	18.0	0.2	2M1207-3932

^a540000+^bSynthetic photometry, calculated by convolving the spectra with Bessell UBVR filter transmission curves for the *Nordic Optical Telescope* at <http://www.not.iac.es/instruments/filters/>^cApproximate flux uncertainty in magnitudes^dAbbreviation for target used throughout this work.^eUsed a 0''.7 slit width.
 TABLE 2
 ARCHIVAL *HST*/STIS G430L OBSERVATIONS

Star	MJD	t_{exp} (s)	Slit	PI	Ref.	Abbreviation
DF Tau	51439.84	144	52 × 0.2	Linsky	2	DF Tau (Sep. 99)
TW Hya	51671.88	260	52 × 0.2	Linsky	1	TW Hya (May 00)
TW Hya	52474.58	120	52 × 0.2	Johns-Krull	-	TW Hya (Jul. 02)
DF Tau	52512.49	120	52 × 0.2	Johns-Krull	-	DF Tau (Aug. 02)
RU Lupi	51737.65	120	52 × 0.1	Walter	2	-
V819 Tau ^a	51786.87	360	52 × 0.1	Walter	2	-
DG Tau	51839.52	240	52 × 0.1	Walter	2	-
V836 Tau	51954.36	360	52 × 0.1	Walter	2	-
LkCa 7A ^a	53039.71	162	52 × 0.2	Johns-Krull	-	LkCa 7

1: Herczeg et al. (2004)

2: Herczeg et al. (2006)

^aWe extract and use only the primary spectrum and do not discuss the faint secondary

TABLE 3
ADOPTED STELLAR PROPERTIES

Star	SpT	log Age ^a log yr	A_V mag	T K	L L_\odot	R R_\odot	M M_\odot	Ref.
CIDA 1	M5	6.0*	3.0	3125	0.21	1.57	0.15	1
GM Tau	M5.5	6.4	2.0	3091	0.070	0.93	0.15	2
2M0414+2811	M6.5	6.5	1.0	2935	0.014	0.46	0.065	3
S0518+2327	M5.5	6.9	1.0	3091	0.016	0.44	0.10	4
MHO 6	M5	6.1	1.0	3125	0.14	1.31	0.17	5
S0439+2336	M5	6.3	0.0	3125	0.089	1.02	0.17	4
2M0436+2351	M5	7.1	1.0	3125	0.013	0.39	0.11	6
2M0441+2534	M7.75	7.0	1.0	2752	0.0033	0.25	0.035	3
2M0444+2512	M7.25	6.6	0.0	2838	0.012	0.45	0.050	3
2M0439+2544	M7.25	6.5	0.8	2838	0.015	0.51	0.050	3
2M1207-3932	M8	7.0	0.0	2550	0.0022	0.24	0.024	7
MHO 5	M6	6.0*	0.3	2990	0.098	1.17	0.10	5
2M0455+3028	M4.75	6.1	1.0	3161	0.15	1.31	0.20	3
CIDA 14	M5.5	6.0	0.3	3058	0.16	1.44	0.12	1
KPNO 11	M5.75	6.5	0.3	3023	0.037	0.70	0.10	8
V927 Tau ^b	M5	6.0*	0.4	3125	0.22	1.60	0.15	9
MHO 7	M5.5	6.3	0.1	3058	0.076	0.99	0.14	5
CFHT 7	M6.5	6.5	0.0	2935	0.025	0.61	0.07	10
<i>HST/STIS</i> Sample								
TW Hya	K7	7.6	0.0	4060	0.17	0.83	0.77	11
RU Lup	K7	7.0	0.1	4060	0.42	1.3	1.0	12
DF Tau ^b	M2	6.0*	0.6	3560	1.45	3.2	0.66	13
DG Tau	K6	7.5	1.3	4205	0.28	1.0	0.85	13
V836 Tau	K7	7.1	1.1	4060	0.32	1.15	0.95	14

1: Briceno et al. (1993)

2: Rydgren & Vrba (1983)

3: Luhman (2004)

4: Slesnick et al. (2006)

5: Briceno et al. (1998)

6: Luhman et al. (2006)

7: Gizis (2002)

^a1 Myr is the youngest age of Baraffe et al. (1998) models.

Ages marked with a "*" are upper limits.

^bBinary, assumes both components have same M , L , and T .

8: Luhman et al. (2003)

9: Herbig et al. (1972)

10: Guieu et al. (2006)

11: Rucinski & Krautter (1983)

12: Henize (1954)

13:Smak (1964)

14:Feigelson & Kriss (1981)

TABLE 4
VEILING MEASUREMENTS OF M-DWARFS FROM *Keck* SPECTRA^a

Star	Template	4227	4955	5450	6190	6880	7100	7800	8600
CIDA 1	V927 Tau	> 2	0.98	0.75	0.94	0.42	0.63	0.38	0.56
		0.85	1.4	2.1	3.6	6.1	8.0	10.9	25.0
GM Tau	MHO 7	> 2	1.84	1.55	3.63	0.88	0.79	0.27	0.26
		0.8	1.2	1.6	2.7	3.7	3.5	2.9	4.7
2M0414+2811	CFHT 7	> 2	> 3	> 3	> 3	1.52	1.59	0.76	0.16
		1.6	2.3	2.5	3.0	4.2	4.3	4.7	2.9
S0518+2327	MHO 7	> 2	1.62	0.79	0.87	0.38	0.38	0.14	0.40
		1.6	1.7	1.4	1.5	1.8	1.9	1.5	5.0
MHO 6	V927 Tau	0.49	0.05	0.03	0.07	0.02	0.01	-0.05	0.02
		0.68	< 0.41	< 0.56	< 0.55	< 0.75	< 1.6	< 1.7	< 2.6
S0439+2336	V927 Tau	0.18	0.05	0.05	0.02	0.02	0.04	0.04	0.13
		0.59	< 0.76	< 1.0	< 1.0	< 1.2	< 2.4	< 2.6	< 3.8
2M0436+2351	V927 Tau	0.36	0.08	0.04	-0.00	-0.02	0.02	-0.07	-0.12
		0.100	0.135	0.092	-0.001	-0.120	0.134	-0.820	-1.817
2M0455+3028	V927 Tau	0.04	0.02	0.03	0.04	0.02	0.02	-0.01	-0.03
		< 0.095	< 0.43	< 0.60	< 0.66	< 0.88	< 1.9	< 2.2	< 3.7
2M0441+2534	2M0439+2544	> 2 ^b	> 3	2.4	4.1	0.50	0.61	0.29	-0.01
		0.04	0.06	0.084	0.14	0.17	0.20	0.24	< 0.085
2M0444+2512	2M0439+2544	2.06 ^b	0.11	0.01	0.06	0.04	0.05	-0.03	0.03
		0.079	0.060	< 0.04	< 0.04	< 0.07	< 0.17	< 0.21	< 0.45
2M1207-3932 (Feb.)	2M0439+2544	0.29 ^b	0.32	0.04	0.59	0.10	0.07	-0.12	-0.01
		0.018	0.069	< 0.017	< 0.015	< 0.038	< 0.084	< 0.11	< 0.28
2M1207-3932 (Nov.)	2M0439+2544	-	0.13	0.05	0.19	0.03	0.01	-0.10	0.01
		-	0.028	< 0.015	< 0.011	< 0.032	< 0.080	< 0.13	< 0.24
MHO 5	CFHT 7	-0.01	-0.02	0.01	0.08	0.03	-0.01	-0.10	-0.03
		< 0.06	< 0.34	< 0.42	< 0.41	< 0.76	< 1.7	< 2.0	< 3.6
CIDA 14	MHO 7	-0.02	-0.00	-0.00	0.01	0.01	-0.01	-0.04	0.05
		< 0.16	< 0.80	< 1.0	< 1.0	< 1.4	< 3.1	< 3.4	< 5.6
KPNO 11	MHO 7	0.06	0.00	-0.06	-0.04	-0.02	-0.03	-0.05	-0.03
		< 0.027	< 0.16	< 0.20	< 0.21	< 0.32	< 0.74	< 0.89	< 1.6
2M0438+2611	2M0439+2544	-	-0.04	-0.29	0.14	0.12	0.04	0.03	0.01
		-	< 0.002	< 0.002	< 0.004	< 0.006	< 0.014	< 0.018	< 0.036
Photospheric Templates									
2M0439+2544	CFHT 7 ^c	0.54	0.06	0.03	0.13	-0.02	-0.02	-0.08	-0.10
		0.011	< 0.013	< 0.020	< 0.023	< 0.052	< 0.13	< 0.17	< 0.38
V927 Tau	MHO 7 ^c	0.04	0.14	0.10	0.06	0.07	0.09	0.10	0.36
		< 0.54	< 2.3	< 2.9	< 3.1	< 3.9	< 8.2	< 8.8	< 13.3
CFHT 7	MHO 7 ^c	0.09	-0.07	-0.09	-0.07	-0.07	-0.07	-0.04	-0.22
		< 0.009	< 0.075	< 0.10	< 0.11	< 0.20	< 0.48	< 0.64	< 1.3
MHO 7	V927 Tau ^c	-0.08	0.08	0.10	0.08	0.08	0.07	-0.09	-0.27
		< 0.093	< 0.44	< 0.55	< 0.54	< 0.77	< 1.7	< 1.9	< 3.4

^aVeiling (accretion continuum flux divided by photospheric continuum flux) at listed wavelength is given on top line
accretion continuum flux (10^{-16} erg cm⁻² s⁻¹ Å⁻¹) given on bottom line for each source.

Flux upper limits are marked with a < and are always calculated for $r_\lambda < 0.05$.

Stars listed in order of \dot{M} (see Table 11).

^bCFHT 7 is used as a template instead of 2M0439+2544 at 4227 Å.

^cMismatched spectral template.

TABLE 5
VEILING MEASUREMENTS FOR HIGHER-MASS ACCRETORS OBSERVED WITH *HST*^a

Star	Template	4000	4600	5400
DF Tau (Sep. 99)	LkCa 7	> 5	1.8	1.3
		310	310	275
DF Tau (Aug. 02)	LkCa 7	> 5	0.73	0.6
		150	126	114
RU Lup	V819 Tau	> 5	1.7	2.3
		840	590	710
DG Tau	V819 Tau	3.0	1.4	1.7
		37	59	64
TW Hya (May 00)	V819 Tau	2.2	0.58	0.36
		510	450	330
TW Hya (Jul. 02)	V819 Tau	1.4	0.69	0.72
		360	460	470
V836 Tau	V819 Tau	0.23	< 0.1	< 0.08
		3.1	< 4.9	< 4.0

^aFormat same as in Table 4

TABLE 6
OBSERVED PROPERTIES OF THE ACCRETION CONTINUUM

Star	J_{obs}^a	J_{mod}^b	S_B^c	F_{4955}/F_{4227}^d
Accretors in <i>Keck I</i> sample				
CIDA 1	3.4	5.6 ± 0.7	4.1 ± 2.0	0.85
GM Tau	3.5	5.9 ± 0.7^e	6.1 ± 1.5	0.9
2M0414+2811	2.7	3.10 ± 0.17	8.1 ± 1.0	1.14
S0518+2327	2.1	2.35 ± 0.15	2.4 ± 2.0	0.83
MHO 6	1.10	3.9 ± 0.8	7.7 ± 1.5	< 0.5
S0439+2336	0.76	3.1 ± 1.5	6.2 ± 1.1	< 1.2
2M0436+2351	1.48	3.8 ± 1.2	–	–
2M0441+2534	2.8	3.75 ± 0.3	7.2 ± 1.0	1.2
2M0444+2512	1.24	3.1 ± 0.7	6.6 ± 1.2	0.76
2M0439+2544	1.37	> 3	16 ± 6	–
2M1207-3932	5.9	15 ± 4	8.7 ± 1.0	–
2M1207-3932	3.4	7 ± 2	10.7 ± 2.0	–
Possible accretors or non-accretors in <i>Keck I</i> sample				
2M0455+3028	0.46	> 1.3	–	–
MHO 5	0.46	> 1.5	–	–
CIDA 14	0.35	–	–	–
KPNO 11	0.41	–	–	–
V927 Tau	0.38	–	–	–
MHO 7	0.34	–	–	–
CFHT 7	0.36	–	–	–
Accretors in <i>HST</i> sample				
DF Tau (Sep. 99)	1.58	1.9 ± 0.1	5.4 ± 0.4	–
DF Tau (Aug. 02)	1.95	2.8 ± 0.3	5.0 ± 0.4	–
RU Lup	1.72	1.9 ± 0.2	2.9 ± 0.5	–
DG Tau	1.35	2.0 ± 0.1	5.2 ± 0.6	–
TW Hya (May 00)	1.66	2.3 ± 0.2	4.3 ± 0.6	–
TW Hya (Jul. 02)	2.0	3.1 ± 0.5	4.8 ± 0.4	–
V836 Tau	0.60	–	–	–
Non-accretors in <i>HST</i> sample				
LkCa 7	0.44	–	–	–
V819 Tau	0.46	–	–	–

^aObserved flux ratio, F_{4000}/F_{3600}

^bFlux ratio, F_{4000}/F_{3600} , after photospheric subtraction and dereddening

^cSlope of Balmer continuum

^dFlux ratio as proxy for slope of Paschen continuum.

^eMeasured at alternate wavelength due to strong line blending

TABLE 7
 BALMER LINE EQUIVALENT WIDTHS AND FLUXES

Star	H α	H β	H γ	H δ	H6	H7	H8	H9	H10	H11	H12
CIDA 1	232 31.2	134 3.0	80 1.08	64 0.65	41 0.38	49 0.38	37 0.29	27 0.24	18 0.21	17 0.20	10 0.14
GM Tau	281 14.6	68 1.11	39 0.41	30 0.24	8.8 0.12	26 0.21	13 0.13	11 0.11	12 0.15	11 0.14	9.1 0.12
2M0414+2811	280 15	103 2.5	72 1.3	58 0.97	30 0.57	32 0.53	23 0.39	17 0.32	10.6 0.26	8.7 0.22	5.6 0.15
S0518+2327	50 2.5	67 1.51	60 1.27	54 1.11	28 0.69	27 0.62	19 0.43	9.8 0.26	5.3 0.18	4.7 0.16	1.9 0.069
MHO 6	55 10.2	31 1.6	37 1.00	28 0.73	27 0.45	27 0.41	21 0.32	16 0.26	12.1 0.19	9.6 0.16	5.3 0.097
S0439+2336	13 3.9	18 1.55	24 1.24	18 0.90	21 0.60	16 0.47	14 0.39	11 0.31	8.9 0.22	6.2 0.16	2.7 0.078
2M0436+2351	28 0.97	47 0.48	74 0.38	62 0.29	46 0.19	44 0.16	32 0.106	16 0.064	10.2 0.046	9.2 0.046	5.7 0.028
2M0441+2534	586 1.7	228 0.16	158 0.085	135 0.061	72 0.036	70 0.029	47 0.020	29 0.014	14.6 0.0101	9.1 0.0070	3.9 0.0035
2M0444+2512	100 1.7	126 0.34	94 0.15	62 0.085	49 0.058	27 0.031	20 0.022	18 0.018	10.3 0.012	B -	B -
2M0439+2544	158 1.7	93 0.12	93 0.054	87 0.035	73 0.022	50 0.016	44 0.012	36 0.0093	36 0.0079	18 0.0056	6.4 0.0027
2M1207-3932 (Feb.)	396 3.7	341 0.53	286 0.27	323 0.20	142 0.124	146 0.099	132 0.084	89 0.066	55 0.050	27 0.037	16 0.027
2M1207-3932 (Nov.)	200 1.21	210 0.19	234 0.119	132 0.088	- 0.071	- 0.052	- 0.042	- 0.037	- 0.024	- 0.0106	- 0.008
2M0438+2611	99 0.16	158 0.023	622 0.013	- 0.0056	- 0.0052	- < 0.0036	- < 0.0036	- < 0.0024	- < 0.0014	- < 0.0014	- < 0.0014
2M0455+3028	9.6 2.12	9.2 0.45	8.6 0.26	6.1 0.15	7.5 0.095	7.1 0.082	4.0 0.051	4.5 0.054	3.0 0.029	2.0 0.018	< 1.0 < 0.012
MHO 5	43 6.6	30 0.83	19 0.34	13.4 0.20	13.1 0.119	10.4 0.084	6.5 0.058	5.7 0.049	5.2 0.029	2.8 0.020	2.1 0.015
CIDA 14	10.2 3.3	7.5 0.54	3.9 0.21	3.4 0.15	3.8 0.083	4.5 0.089	1.4 0.032	2.2 0.048	< 5.4 0.07	< 3.8 < 0.05	< 3.8 < 0.05
KPNO 11	13.6 1.03	12.5 0.18	9.5 0.087	7.6 0.054	8.4 0.033	7.4 0.028	3.3 0.014	3.6 0.014	3.5 0.010	< 1.6 < 0.005	< 1.6 < 0.005
V927 Tau	10.7 10.2	7.9 1.9	3.7 0.71	3.2 0.46	3.6 0.26	3.9 0.25	1.6 0.12	2.2 0.15	2.1 0.11	< 1.7 < 0.08	< 1.7 < 0.08
MHO 7	7.4 1.31	5.4 0.22	2.5 0.079	1.9 0.049	2.0 0.026	< 2.5 < 0.03	< 1.5 < 0.02	1.6 0.021	< 5.7 < 0.04	< 1.7 < 0.012	< 2.0 < 0.015
CFHT 7	15 0.63	14 0.084	14 0.042	8.5 0.021	7.4 0.0115	5.3 0.0082	2.5 0.004	3.5 0.005	6.0 0.0005	- < 0.003	- < 0.003

Table 7 (continued): *HST*/STIS Sample

Star	H α	H β	H γ	H δ	H6	H7	H8	H9	H10	H11	H12
DF Tau	-	29	27	26	22	17	13	8.4	5.2	3.4	2.9
(Sep. 99)	-	150	109	90	68	54	42	30	19	13	11.5
DF Tau	-	26	20	17.7	16	15	10.9	7.8	6.1	3.9	4.2
(Aug. 02)	-	80	44	32	24	24	16	13.6	11.3	7.6	7.9
RU Lupi	-	37	16	14.5	7.3	8.7	6.6	9.3	4.6B	4.4	3.0
	-	360	160	113	68	74	57	80	51B	48	33
DG Tau	-	24	14	11.6	8.8	11.8	6.9	4.2	3.6	2.5	5.3
	-	29	11.5	7.0	4.2	5.1	3.1	2.1	1.9	1.4	2.5
TW Hya	-	38	28	28	24	20	14	9.5	7.0	4.1	5.0
(May 00)	-	470	280	230	160	137	104	76	57	37	42
TW Hya	-	77	48	42	33	26	18	12	7.6	5.3	3.6
(Jul. 02)	-	880	420	290	190	150	113	84	58	43	30
V836 Tau	-	17	8.8	9.4	13	9.6	7.5	1.0	6.2	5.1	3.4
	-	9.6	3.1	2.0	1.3	0.84	0.70	0.85	0.45	0.35	0.25
V819 Tau	-	< 0.8	< 2	< 1.8	< 4	< 7	< 2	< 6	< 6	< 6	-
	-	< 1.3	< 1.6	< 0.9	< 0.8	< 0.6	< 0.4	< 1.0	< 0.6	< 0.8	-
LkCa 7	-	1.8	< 3	2.0	3.2	4.7	1.9	< 5.5*	< 5	< 7	-
	-	4.8	< 6	2.2	1.5	1.6	0.86	< 2.2*	< 1.5	< 2.5	-

^aEquivalent width (-Å) in first row, flux (10^{-14} erg cm $^{-2}$ s $^{-1}$) in second row for each star.

B=blend, *=marginal detection, ID=questionable line identification

TABLE 8
 HE LINE EQUIVALENT WIDTHS AND FLUXES^a

Star	$\lambda 4026$	$\lambda 4470$	$\lambda 4922$	$\lambda 5016$	$\lambda 5876$	$\lambda 6678$	$\lambda 7065$	He II $\lambda 4686$
<i>Keck I/LRIS sample of low-mass stars</i>								
CIDA 1	4.3B 0.035B	5.3 0.086	8.3 0.22	10.4 0.26	9.6 0.49	1.9 0.22	2.0 0.31	1.3 0.23
GM Tau	2.5 0.019B	5.0 0.055ID	13.9 0.23	16.1 0.26	4.6 0.12	1.1 0.052	0.5 0.030	0.2 0.015
2M0414+2811	2.8 B 0.038 B	4.2 0.085	8.2 0.20	9.6 0.24	7.3 0.23	2.4 0.11	1.5 0.084	1.1 0.062
S0518+2327	3.5 0.064	5.7 0.12	2.8 0.071	3.4 0.078	7.7 0.19	2.4 0.087	0.9 0.041	1.5 0.033
MHO 6	1.9 0.047	2.1 0.082	0.6 0.041	0.9 0.044	2.9 0.19	0.5 0.060	0.6 0.10	0.5 0.023
S0439+2336	1.2 0.054	1.2 0.094	0.3 0.033	0.4 0.038	1.5 0.18	0.4 0.084	< 0.2 < 0.07	0.1 0.011
2M0436+2351	3.8 0.018	3.8 0.028	0.95 0.012	< 0.75* < 0.009*	2.9 0.052	1.7 0.036	2.3 0.103	0.84 0.0076
2M0441+2534	8.1 0.0030	16.2 0.0084	6.8 0.0051	7.5 0.0058	29 0.041	8.5 0.021	3.6 0.013	2.1 0.0012
2M0444+2512	3.9 0.0053	7.2 0.014	1.5 0.0063	4.9 0.014	12.4 0.054	1.4 0.014	0.7 0.013	2.1 0.0049
2M0439+2544	4.6 0.0022	8.7 0.0062	1.0 0.0022	2.3 0.0031	11.2 0.028	1.8 0.013	0.5 0.0075	1.5 0.0015
2M1207-3932 (Feb.)	8.8 0.0074	22 0.021	2.5 0.0056	3.6 0.0057	33 0.075	4.2 0.022	1.6 0.014	3.1 0.0039
2M1207-3932 (Nov.)	< 6.5 < 0.004*	267 0.017	3.7 0.0069	4.5 0.0053	21 0.038	3.5 0.015	1.2 0.010	< 3.1 < 0.0034
2M0438+2611	– < 0.003	– < 0.003	– < 0.002	– < 0.002	< 10 < 0.004	< 2 < 0.0015	< 1.8 < 0.0025*	– < 0.002
2M0455+3028	0.3 0.0081	< 0.17 < 0.007*	0.1 0.0070	0.1 0.0056	0.4 0.030	< 0.13 < 0.02*	< 0.3 < 0.06	< 0.08 < 0.004
MHO 5	< 0.8* < 0.014	< 1.0* < 0.020	< 0.4* < 0.022	< 0.4* < 0.042	1.3 0.0555	< 0.25* < 0.025	< 0.16* < 0.025	< 0.25 < 0.006
CIDA 14	< 0.3 < 0.015	< 0.18 < 0.012	< 0.1 < 0.012	0.1 < 0.009	0.3 0.037	< 0.07 < 0.016	< 0.1 < 0.04	< 0.10 < 0.007
KPNO 11	0.4 0.0033	0.4 0.0053	0.2 0.0059	< 0.18 < 0.003	0.4 0.0092	0.1 0.0061	< 0.2 < 0.015	< 0.10 < 0.0015
V927 Tau	< 0.15 < 0.02	< 0.4 < 0.08	< 0.15 < 0.06	< 0.02 < 0.06	0.30 0.11	< 0.2 < 0.12	< 0.2 < 0.18	< 0.25 < 0.06
MHO 7	< 0.18 < 0.005	< 0.33 < 0.013	< 0.25 < 0.02	< 0.30 < 0.014	< 0.20 < 0.012	< 0.27 < 0.035	< 0.17 < 0.035	< 0.2 < 0.008
CFHT 7	< 0.45 < 0.0015	< 0.4 < 0.002	0.20 0.0027	< 0.26 < 0.002	0.35 0.0042	0.13 0.0035	< 0.3 < 0.015	< 0.4 < 0.002*

Table 8 (continued)

Star	$\lambda 4026$	$\lambda 4470$	$\lambda 4922$	$\lambda 5016$	$\lambda 5876$	$\lambda 6678$	$\lambda 7065$	He II $\lambda 4686$
<i>HST/STIS sample of higher mass stars</i>								
DF Tau	1.9	2.8	2.0	1.3	–	–	–	0.7
Sep. 99	6.1	12.4	10.8	6.6	–	–	–	3.3
DF Tau	1.7	1.3	2.4	2.6	–	–	–	0.4
Aug. 02	2.8	3.5	8.3	7.9	–	–	–	1.13
RU Lupi	3.3B 25B	3.3 33	9.5 90	9.5 92	– –	– –	– –	< 0.35* < 3.2*
DG Tau	1.3 0.65	1.7 1.5	3.2 3.9	4.4 5.0	– –	– –	– –	< 0.5 < 0.5
TW Hya	2.2	2.8	0.9	1.0	–	–	–	1.1
May 00	16.8	29.8	10.9	11.8	–	–	–	14.1
TW Hya	2.3	2.9	1.5	1.2	–	–	–	1.0
Jul. 02	14.9	28	17	12.8	–	–	–	11.4
V836 Tau	1.1 0.18	0.6 0.26	0.7 0.40	0.3 0.19	– –	– –	– –	0.5 0.27
V819 Tau	< 2.5 < 1.0	< 1.5 < 1.5	< 1.4 < 2.0	< 0.7 < 1.0	– –	– –	– –	< 1.0 < 1.5
LkCa 7	< 2.8 < 2.0	< 1.5 < 2.5	< 1.2 < 3.0	< 0.4 < 1.0	– –	– –	– –	< 1.2 < 3.0

^aEquivalent width and line flux format as in Table 4.

B=blend, *=marginal detection, ID=questionable line identification

TABLE 9
 CA AND NA LINE EQUIVALENT WIDTHS AND FLUXES

Star	Ca II K	Ca II H ^c	Ca II λ 8498	Ca II λ 8542	Ca II λ 8662	Na I λ 5893	O I λ 7773	O I λ 8446
CIDA 1	175	160	14.7	18.9	14.4	10.4	1.7	2.5
	1.49	1.32	7.8	10.4	9.1	0.48	0.54	1.36
GM Tau	106	135	28	29	21	15.4	1.14	3.4
	1.35	1.15	4.4	4.5	4.1	0.41	0.114	0.55
2M0414+2811	116	142	39	40	30	11	1.24	2.0
	1.9	2.3	4.9	5.4	5.1	0.35	0.108	0.28
S0518+2327	20	59	1.73	2.1	1.94	4.35	2.30	1.23
	0.43	1.21	0.22	0.27	0.32	0.093	0.19	0.15
MHO 6	30	43	< 0.9	< 1.5	< 0.4	0.98	< 0.4	< 0.5
	0.45	0.92	< 0.4	< 0.7	< 0.3	0.048	< 0.14	< 0.24
S0439+2336	23	35	< 0.08	< 0.15	< 0.09	< 0.36	0.16	< 0.17
	0.59	1.21	< 0.06	< 0.11	< 0.08	< 0.04	0.083	< 0.13
2M0436+2351	41	79	1.7	1.6	1.1	2.2	1.1	< 0.5
	0.13	0.35	0.15	0.16	0.12	0.039	0.065	< 0.5
2M0441+2534	53	160	6.6	6.4	5.0	11.4	1.14	1.29
	0.021	0.062	0.094	0.107	0.123	0.016	0.0090	0.019
2M0444+2512	49	83	< 0.6*	0.45	0.29	20	< 0.4	< 0.6
	0.053	0.101	< 0.04*	0.030	0.028	0.068	< 0.016	< 0.05
2M0439+2544	38	93	< 0.8	< 1.1	< 0.8	4.8	< 0.4	< 1.1
	0.013	0.037	< 0.05	< 0.07	< 0.08	0.0088	0.013	< 0.08
2M1207-3932 (Feb.)	36.36	196.32	< 0.7	< 1.6	< 0.8	5.4	2.02	1.95
	0.024	0.178	< 0.03	< 0.076	< 0.05	0.013	0.048	0.082
2M1207-3932 (Nov.)	90	200	< 1.3	< 0.9	< 0.9	4.7	< 0.9	< 1.3
	0.012	0.071	< 0.06	< 0.05	< 0.03	0.008	< 0.02	< 0.06
2M0438+2611	–	34	< 1.3	< 1.2	< 0.8	< 17	< 0.9	< 0.9
	–	0.0053	< 0.008	< 0.008	< 0.007	< 0.007	< 0.003	< 0.005
2M0455+3028	30	26	< 0.3	< 0.3	0.31	0.16	< 0.11	< 0.35
	0.37	0.43	< 0.21	< 0.23	0.28	0.009	< 0.049	< 0.25
MHO 5	48	42	< 1.3	< 0.8	< 0.7	1.6	< 0.2	< 0.5
	0.43	0.51	< 0.8	< 0.5	< 0.6	0.046	< 0.07	< 0.3
CIDA 14	14.3	11.9	< 0.10	< 0.15	< 0.10	0.86	< 0.12	< 0.15
	0.30	0.34	< 0.10	< 0.14	< 0.13	0.057	0.080	< 0.22
KPNO 11	32	26	< 0.25	< 0.31	0.28	< 0.20	< 0.12	< 0.26
	0.125	0.143	< 0.07	< 0.09	0.123	< 0.004	< 0.021	< 0.08
V927 Tau	24	18.4	< 0.21	< 0.17	< 0.13	< 0.20	< 0.13	< 0.34
	1.55	1.63	< 0.5	< 0.4	< 0.40	< 0.06	< 0.31	< 0.9
MHO 7	13	10	< 0.2	< 0.2	< 0.2	< 0.2	< 0.2	< 0.4
	0.17	0.18	< 0.10	< 0.11	< 0.14	< 0.011	< 0.08	< 0.27
CFHT 7	27	21	< 0.4	< 0.4	0.21	< 0.4	< 0.2	< 0.6
	0.043	0.047	< 0.09	< 0.09	0.064	< 0.004	< 0.025	< 0.14

^aEquivalent width and line flux format as in Table 4.

B=blend, *=marginal detection, ID=questionable line identification

^cBlended with He

TABLE 10
WIND LINE EQUIVALENT WIDTHS AND FLUXES

Star	O I λ 6300	O I λ 6363	O I λ 5577	S II λ 6716	S II λ 6731	Fe II λ 7155	S II λ 4069	S II λ 4076
CIDA 1	1.17 0.084	<0.32 <0.029	0.48 0.0096	<0.28 <0.030	0.21 0.023	<0.30* <0.042*	<3.5B <0.034B	<2.7B <0.028B
GM Tau	5.4 0.19	2.0 0.077	1.9 0.052	0.34 0.015	0.64 0.030	<0.27* <0.015*	<7.5B <0.069B	<5.0B <0.040B
2M0414+2811	3.2 0.12	1.17 0.047	1.01 0.033	0.42 0.020	0.17 0.0078	0.15 0.0081	<2.8B <0.047B	<2.8B <0.049B
S0518+2327	1.02 0.028	0.44B 0.014B	1.30 0.035	<0.21* <0.0069*	<0.17 <0.0057	0.25 0.0099	<0.63 <0.0127	<1.47B <0.030B
MHO 6	0.88 0.075	0.17 0.021	0.18 0.021	<0.12 <0.014	<0.31 <0.036	<0.24 <0.032	6.0 0.15	2.2 0.051
S0439+2336	0.46 0.068	<0.18 <0.037	0.17 0.028	<0.21 <0.040	<0.15 <0.028	<0.18 <0.041	0.68 0.031	0.53 0.024
2M0436+2351	< 1.0 < 0.015	< 0.3	< 1.4 < 0.019	< 1.5 < 0.03	< 0.2 < 0.005	< 0.7 < 0.02	< 2.0 < 0.011	< 2.0 < 0.011
2M0441+2534	8.3 0.015	2.3 0.0048	4.3 0.0011	<1.02* <0.0026*	<0.67* <0.0017*	<0.26 <0.0008	<5.29 <0.0023	<2.60 <0.0012
2M0444+2512	62 0.40	13.2 0.13	6.6 0.038	16 0.13	29 0.27	0.68 0.0094	413 0.56	129 0.16
2M0439+2544	1.51 0.0060	<0.36 <0.0023	1.75 0.0071	<0.93 <0.0059	<0.18 <0.0012	<0.18 <0.0016	<1.39 <0.0006	<1.66 <0.0008
2M1207-3932 (Feb.)	< 2.3 < 0.006	< 0.7 < 0.003	2.4 0.0059	< 0.47 < 0.0022	< 0.44 < 0.0022	< 0.38 < 0.0024	< 3.30 < 0.0026	7.1 0.0062
2M1207-3932 (Nov.)	< 5.0 < 0.013	< 0.91 < 0.0035	1.6 0.0015	< 0.53 < 0.0021	< 0.36 < 0.0015	< 0.36 < 0.0020	< 8.14 < 0.0047	< 7.46 < 0.0048
2M0438+2611	98 0.048	20 0.0149	20 0.0052	5.0 0.0037	8.6 0.0072	<2.3 <0.0023	- 0.0106	- 0.0018
2M0455+3028	<0.06 <0.0066	<0.09 <0.0124	0.27 0.0112	<0.20 <0.028	<0.11 <0.0147	<0.12 <0.021	<0.22 <0.0052	<0.14 <0.0034
MHO 5	1.64 0.101	0.35 0.033	<0.58 <0.034	<0.11* <0.0103*	<0.09 <0.0082	<0.23 <0.027	<0.52 <0.0083	<0.45 <0.0072
CIDA 14	0.27 0.040	<0.12 <0.026	<0.12 <0.019	<0.06 <0.012	<0.06* <0.013*	<0.08 <0.021	<0.15 <0.0068	<0.19 <0.0084
KPNO 11	<0.23 <0.0073	<0.08 <0.0040	<0.50 <0.0145	<0.09 <0.0039	<0.12 <0.0056	<0.13 <0.0072	<0.40 <0.0029	<0.34 <0.0025
V927 Tau	<0.17 <0.081	<0.16 <0.108	<0.41 <0.19	<0.11 <0.069	<0.11 <0.064	<0.07 <0.052	<0.25 <0.037	<0.28 <0.040
MHO 7	<0.22 <0.0175	<0.07 <0.0086	<0.38 <0.032	<0.20 <0.021	<0.16 <0.018	<0.20 <0.027	<0.28 <0.0073	<0.13 <0.0033
CFHT 7	<0.24 <0.0042	<0.18 <0.0048	<1.09 <0.0156	<0.15 <0.0036	<0.16 <0.0041	<0.27 <0.0091	<0.58 <0.0016	<0.31 <0.0009

^aEquivalent width and line flux format as in Table 4.

B=blend, *=marginal detection, ID=questionable line identification

Tables 9 and 10 (continued for *HST* Sample)

Star	Ca II K	Ca II H ^c	[O I] λ 5577	[S I] λ 4069 + 4076 ^d
DF Tau	10.4	30	0.7	< 1.5
Sep. 99	31	92	6.6	< 4.7
DF Tau	28	38	0.9	3.0
Aug. 02	42	56	4.1	4.7
RU Lupi	50	39	< 0.3	9.2
	500	330	< 3	72
DG Tau	61	44	0.39	19 ^e
	33	22	0.67	9.2 ^e
TW Hya	9.6	32.0	< 0.15	< 0.8
May 00	65	230	< 2.5	< 6.0
TW Hya	11.5	45	< 0.15	< 0.7
Jul. 02	65	270	< 2.0	< 4.0
V836 Tau	12.9	19.5	< 0.26*	4.1
	1.37	2.6	< 0.24*	0.79
V819 Tau	4.1	4.2	< 0.5	< 1.7
	0.95	1.2	< 1.2	< 0.8
LkCa 7	7.9	7.0	< 0.5	< 2.5
	3.8	4.2	< 2.0	< 2.0

^aEquivalent width and line flux format as in Table 4.

B=blend, *=marginal detection, ID=questionable line identification

^cBlended with He

^dLines are marginally resolved and are coadded here

^eEmission extended by 0".3 in slit and included in extraction

TABLE 11
 MODEL ACCRETION PARAMETERS

Star	Template	T K	n_e 10^{14} cm^{-3}	L 10^7 cm	δ %	r_{3600}	r_{4000}	L_{acc} $10^{-4} L_{\odot}$	\dot{M}_{acc} $10^{-10} M_{\odot} \text{ yr}^{-1}$
Low-mass accretors in <i>Keck I</i> sample									
CIDA 1	V927 Tau ^a	10500	0.8	10	1.01	70	4	280	120
GM Tau	MHO 7	9000	0.7	20	0.53	110	4.9	81	20
2M0414+2811	CFHT 7	7400	2.5	2	3.3	200	20	32	9.0
S0518+2327	MHO 7	10500	2.5	1	0.59	68	6.7	28	5.0
MHO 6	V927 Tau	7800	1.5	8	0.31	3.4	0.29	14	4.4
S0439+2336	V927 Tau	8300	2.0	3	0.12	1.4	0.15	6.5	1.5
2M0436+2351	V927 Tau	(9500)	1.3	1.	1.7	5.0	0.35	3.8	0.53
2M0441+2534	CFHT 7	8000	1.5	5	0.38	40	3.9	0.67	0.19
2M0444+2512	CFHT 7	8200	2.0	2.5	0.034	3.5	0.20	0.26	0.092
2M0439+2544	CFHT 7	(7500)	(1.0)	20	0.19	3.4	0.14	0.17	0.069
2M1207-3932(Feb.)	CFHT 7	7500	0.3	7	1.00	26	0.8	0.061	0.023
2M1207-3932(Nov.)	CFHT 7	6500	1.5	20	1.4	21	0.7	0.044	0.017
Possible accretors in <i>Keck I</i> sample									
2M0455+3028	V927 Tau	(9500)	(2.0)	1.5	0.007	0.4	0.06	1.7	0.58
MHO 5	CFHT 7 ^b	(8500)	(2.0)	2	0.006	0.22	0.02	0.46	0.22
CIDA-14	MHO 7	(9500)	(2.0)	5	0.002	0.14	0.013	0.29	0.14
KPNO 11	MHO 7 ^c	(8500)	(2.0)	6	0.008	0.54	0.04	0.23	0.062
V927 Tau	MHO 7	(9500)	(2.0)	3	0.001	0.24	0.05	3.4 ^d	1.3 ^d
Accretors in <i>HST</i> sample									
DF Tau (Sep. 99)	LkCa 7	8500	3.0	2.0	7.0	16	4	2400	460
DF Tau (Aug. 02)	LkCa 7	9000	1.6	4.0	2.5	10	1.8	1200	230
RU Lupi	V819 Tau	9200	2.0	1.7	28	75	13	3500	180
DG Tau	V819 Tau	8200	2.2	12	19	12	2.5	870	41
TW Hya (May 00)	V819 Tau	9000	2.0	1.5	12	12	2.2	360	15.4
TW Hya (Jul. 02)	V819 Tau	9000	1.8	1.0	12	12	1.7	340	14.6
V836 Tau	V819 Tau	(9000)	(2.0)	0.5	1.4	0.65	0.1	32	1.5

^aThe photospheric template of V927 Tau is adjusted slightly by adding the spectrum of MHO 7

^bIncreased the flux of the template CFHT 7 by assuming $A_V = 1$ to account for the spectral type discrepancy.

^cDecreased the flux of the template MHO 7 by assuming $A_V = 0.3$ to account for the spectral type discrepancy.

^dTotal L_{acc} and \dot{M} for both components.

^fFrom Briceno et al. (2002)

 TABLE 12
 ERROR ESTIMATES

Parameter	Uncertainty	Dependent Variables	$\log(\sigma\dot{M})^a$	Systematic
A_V	0.5 mag	L_{acc}	0.4	?
SpT	0.5 classes	M, R	0.14	No?
Pre-main sequence track	0.03–0.4 dex	M	–0.03 to –0.4	Yes
Mass calibration	0.2 dex	M	0 to –0.2	Yes
Distance	15 pc	L_{acc}^2, R	0.13	No?
Exclusion of lines	$0.25L_{acc}$	L_{acc}	+0.03 to +0.25	Yes
Flux Calibration	0.18 dex	$\propto L_{acc}, R^{1/2}$	0.26	Sometimes
Bolometric Correction	0.3 dex	L_{acc}	+0.3	Yes
Truncation Radius	0.3 dex	R_{in}	0.08	?
Photospheric Template	0–0.3 dex	L_{acc}	0 to +0.3	No?
Single/binary	0.15 dex	R	–0.3	Yes
Re-radiation of emission	0.3 dex	L_{acc}	+0.3	Yes

^a+ or – indicates that the uncertainty is only in one direction.

 TABLE 13
 ESTIMATED \dot{M} FROM V-BAND EXCESS^a

Star	V	M	R	r_V	A_V	f_{5500}	L_{acc}	\dot{M}
Star	mag	M_{\odot}	R		mag	$10^{-16} \text{ erg cm}^{-2} \text{ s}^{-1} \text{ AA}^{-1}$	$10^{-4} L_{\odot}$	$10^{-10} M_{\odot} \text{ yr}^{-1}$
GM Tau	17.577	0.15	0.93	1.7 ± 0.9	2.0	13	79	19
KPNO 12	23.228	0.014	0.14	5_{-2}^{+3}	1.6	0.067	0.41	0.16
KPNO 4	24.722	0.01	0.42	1.6 ± 0.8	4.0	0.11	0.67	1.1
KPNO 6	22.292	0.02	0.68	$1.1_{-0.7}^{+0.9}$	0.7	0.044	0.27	0.36

^aMagnitudes, Excess, and stellar properties (except for GM Tau) from Kraus et al. (2006).

TABLE 14
COMPARING \dot{M} MEASURED FROM UV EXCESS AND H α

Star	H α Profile ^a			UV Excess ^b		Ref
	H α 10% width (km s ⁻¹)	H α EW (Å)	log \dot{M} (log M_{\odot} yr ⁻¹)	H α EW (Å)	log \dot{M} ^c (log M_{\odot} yr ⁻¹)	
MHO 5	154	-60	-10.8	-43	-10.7	1
MHO 6	309	-25	-10.3	-55	-9.3	1
CIDA 14	289	-34	-10.3	-10	-10.9	1
2M0414+2811	362	-250	-10	-288	-8.9	2
2M0439+2544	215	-102	-11.3	-161	-11.1	2
2M0441+2534	256	-234	-11.3	-600	-10.5	2
2M0455+3028	320	-24.5	–	-9.5	< -10.5	2
TW Hya	361	–	-9.3	–	-8.7	3
KPNO Tau 12	206	-66.8	-11.4	–	-10.8 ^f	2
KPNO Tau 4	192	-38.4	< -12	–	-10.0 ^{f,g}	2
KPNO Tau 6	235	-41.1	-11.4	–	-11.0 ^f	2
CIDA 1	375	126	–	232	-7.9	4
GM Tau	370	113 ⁱ	–	281	-8.7	4
2M1207-3932	280	–	–	200,400	-11.7	5,6
KPNO 11	182	17.7 ^h	–	13.6	< -11.2	5
V927 Tau	290	7.0	–	10.7	< -9.9	1
MHO 7	116	9.0	–	7.4	–	1

1: Muzerolle et al. (2003)

4: White & Basri (2003)

2: Muzerolle et al. (2005)

5: Mohanty et al. (2005)

3: Muzerolle et al. (2000)

6: Schaefer et al. (2006)

^aMeasured during H α \dot{M} measurement^bMeasured during UV excess \dot{M} measurement^cMay differ from Table 10, M_* and R_* adopted here from Muzerolle et al.^fCalculated from V-band excess, see §5.1^g M , R from Table 14

TABLE 15
LINE LUMINOSITY-ACCRETION LUMINOSITY RELATIONSHIPS FOR SELECTED LINES

Diagnostic	λ (Å)	a ^a	b ^a	# ^b	σ ^c
He I	5016	3.3 ± 0.3	1.04 ± 0.05	18	0.30
He I	5876	5.3 ± 0.7	1.46 ± 0.12 ^d	12	0.34
He II	4686	3.7 ± 0.5	1.04 ± 0.08	16	0.38
Na I D	5893	3.3 ± 0.7	1.09 ± 0.11	11	0.41
Ca II	8542	2.5 ± 0.5	1.02 ± 0.11	20	0.44
O I	6300	2.8 ± 0.8	0.96 ± 0.16	26	0.67
H α	6563	2.0 ± 0.4	1.20 ± 0.11	35	0.57
H β	4861	2.6 ± 0.2	1.22 ± 0.05	19	0.26
H γ	4340	3.0 ± 0.2	1.24 ± 0.04	19	0.21
Ca II K	3932	2.0 ± 0.3	0.96 ± 0.05	19	0.33
H-9	3771	3.4 ± 0.2	1.17 ± 0.03	19	0.18

^a log $L_{line} = a + b \log L_{acc}$, with L_{acc} and L_{line} in units of L_{\odot} ^bNumber of accretors with detections.^cStandard deviation of detected line fluxes from linear fit.^dSignificant deviation from 1.0, use with caution outside our \dot{M} range.

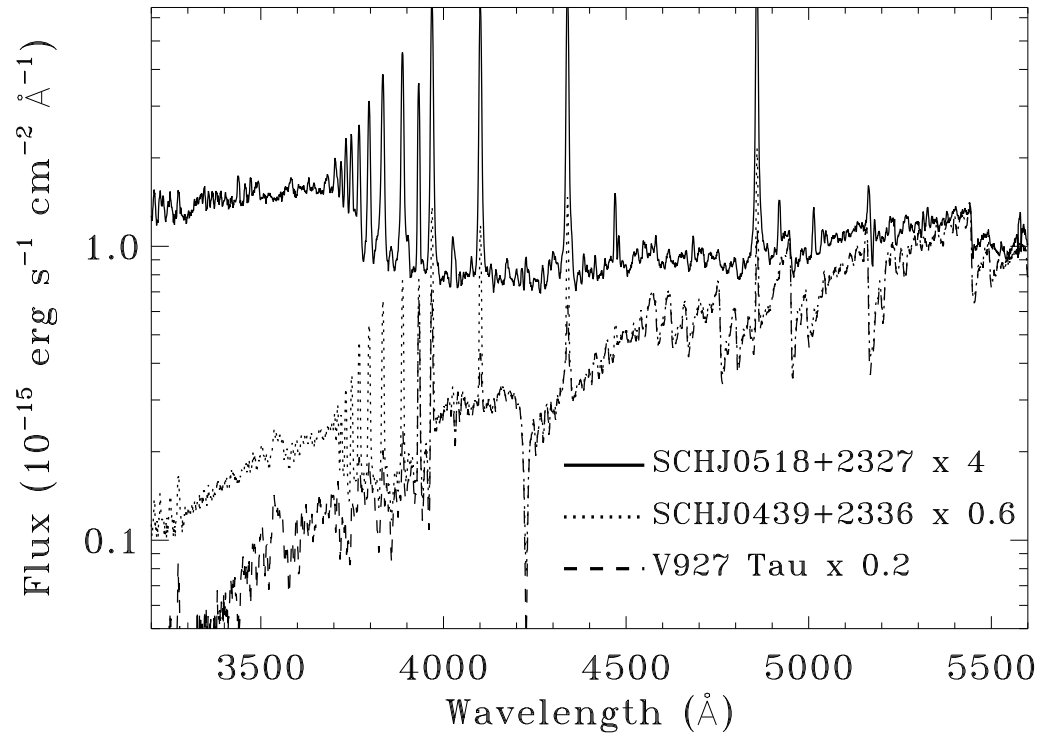


FIG. 1.— Three spectra at 3300–5600 Å. The spectrum of V927 Tau is dominated by photospheric emission, with strong TiO bands and Ca I λ 4227 absorption line. Moderate accretors, such as S0439+2336, are dominated by photospheric emission longward of the Balmer jump at 3700 Å but excess Balmer continuum emission at shorter wavelengths. The TiO bands at < 5600 Å are only weakly detected from the strong accretor S0518+2327, which shows a heavily veiled spectrum both shortward and longward of the Balmer jump.

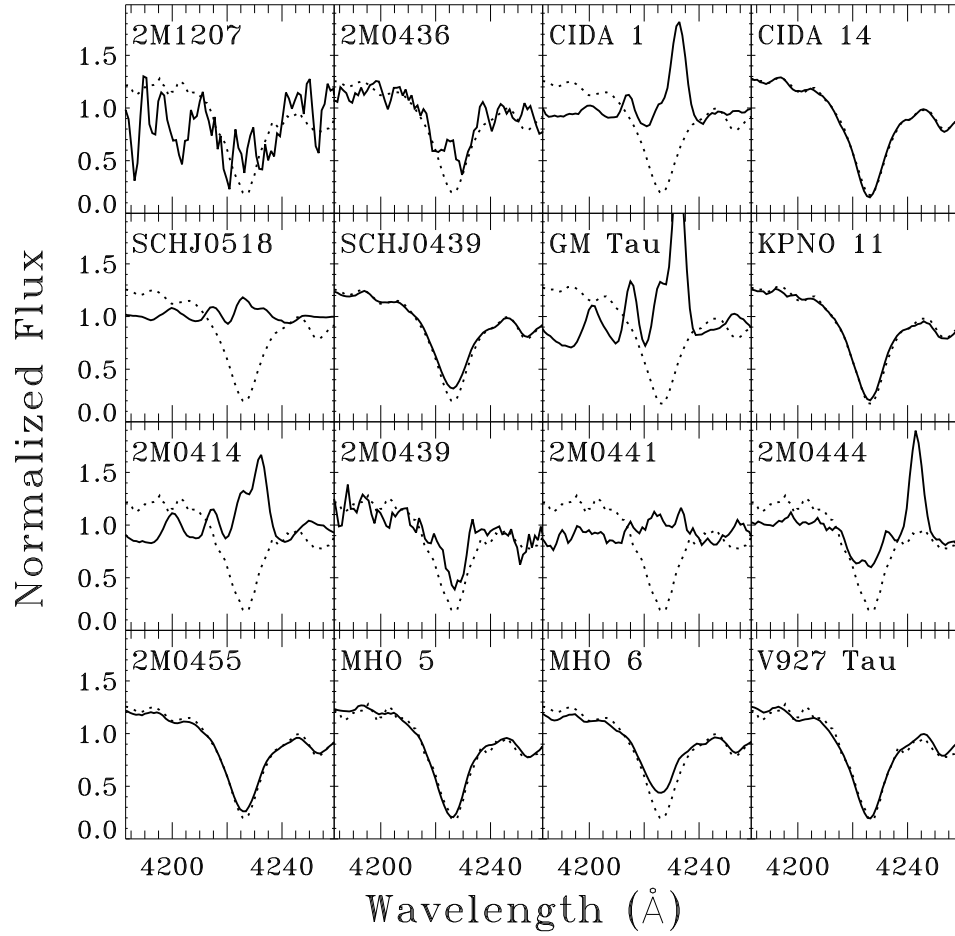


FIG. 2.— The Ca I $\lambda 4227$ absorption line in our LRIS spectra (solid lines) compared with a photospheric template (dotted lines, template listed in Table 5). When present, accretion fills in some of the absorption. The veiling is calculated from the depth of the absorption line. Emission lines in the vicinity of the Ca I $\lambda 4227$ line from several strong accretors (e.g., CIDA 1, GM Tau) limit our ability to measure high veilings and may lead to overestimated small veilings.

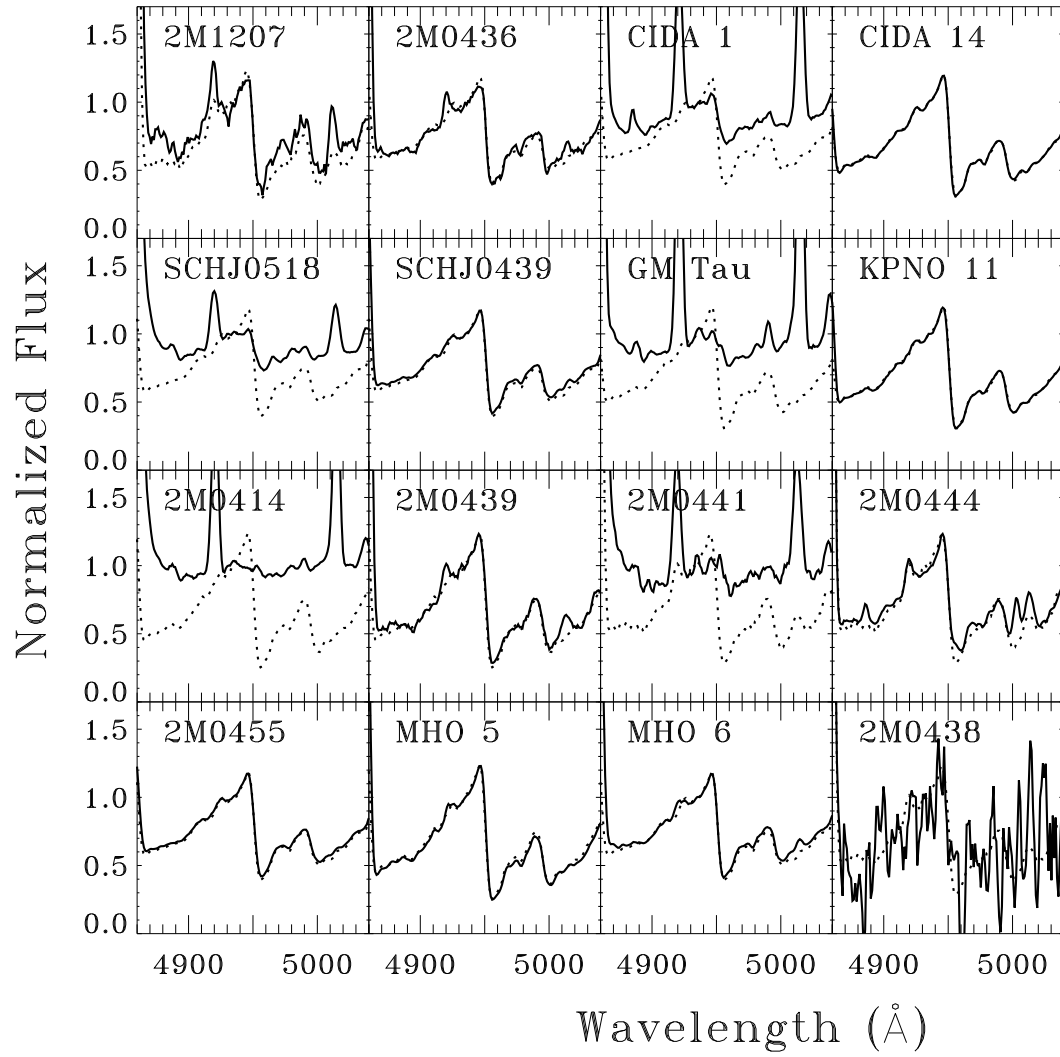


FIG. 3.— A TiO absorption band at 4955 Å used for veiling measurements.

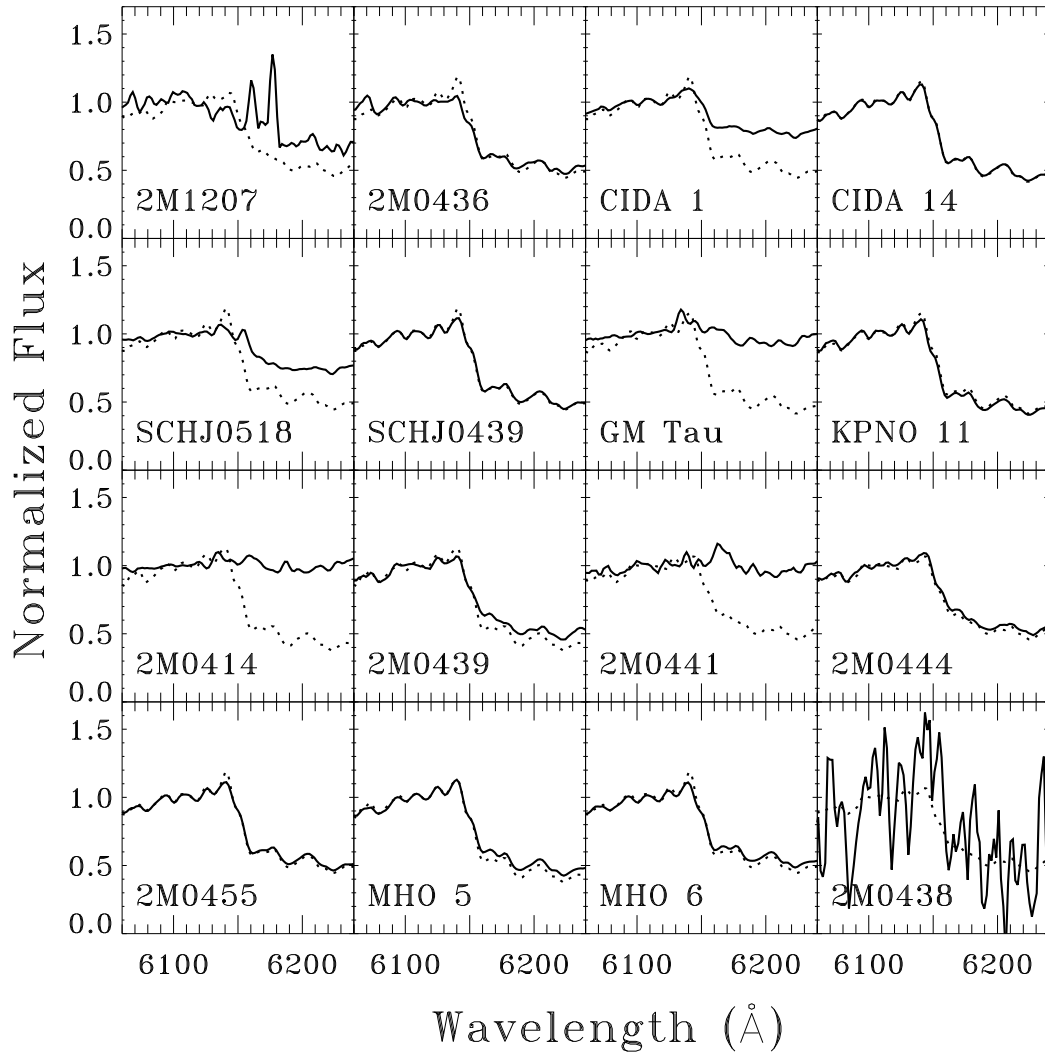


FIG. 4.— A TiO absorption band at 6150 Å used for veiling measurements.

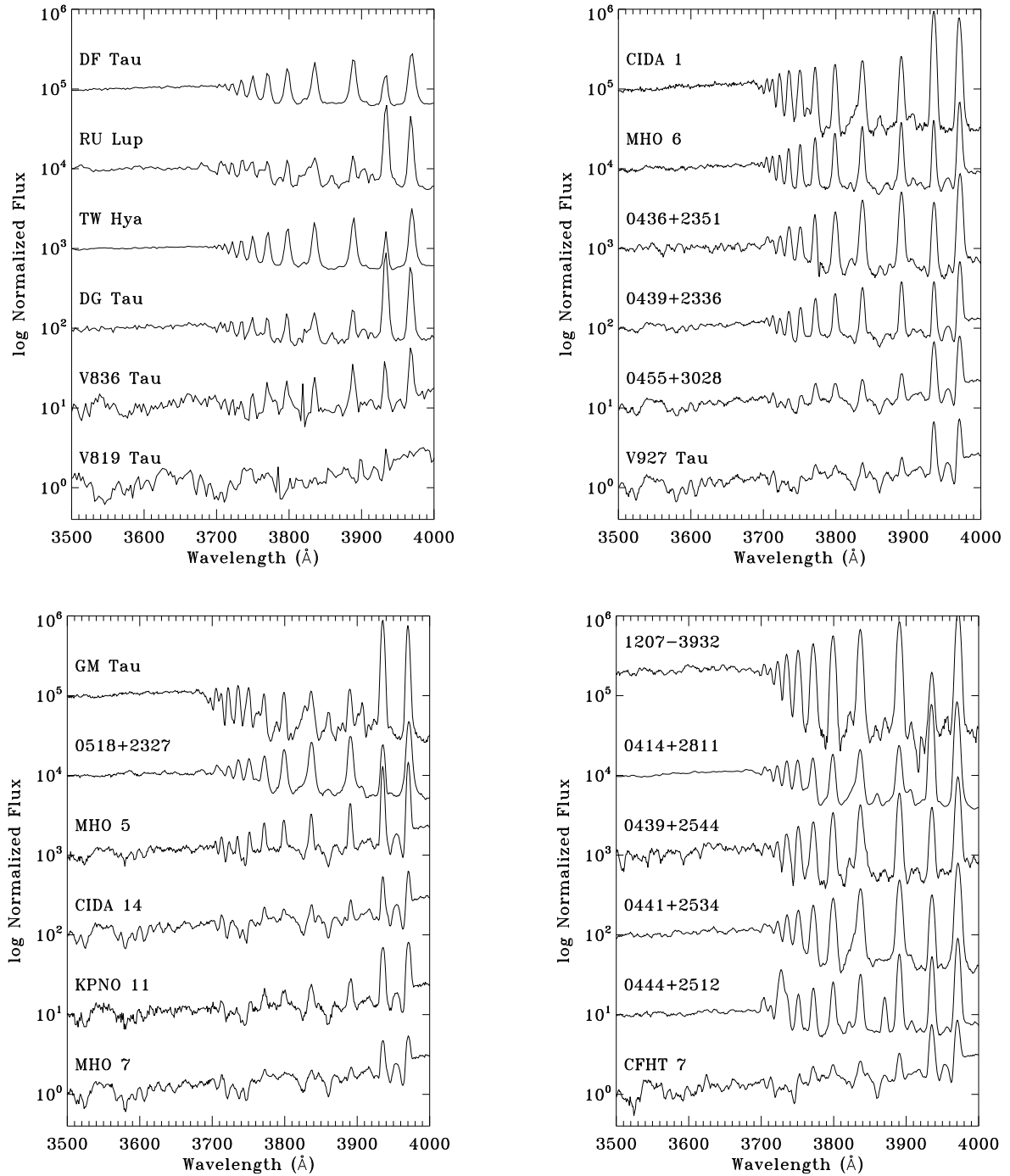


FIG. 5.— The spectral region from 3500–4000 Å for late-K/early M stars (upper left), M5 stars (upper right), M5.5-M6 stars (lower left), and M6.5-M8 stars (lower right). The Balmer continuum, Balmer series, and Ca II H & K are apparent in emission.

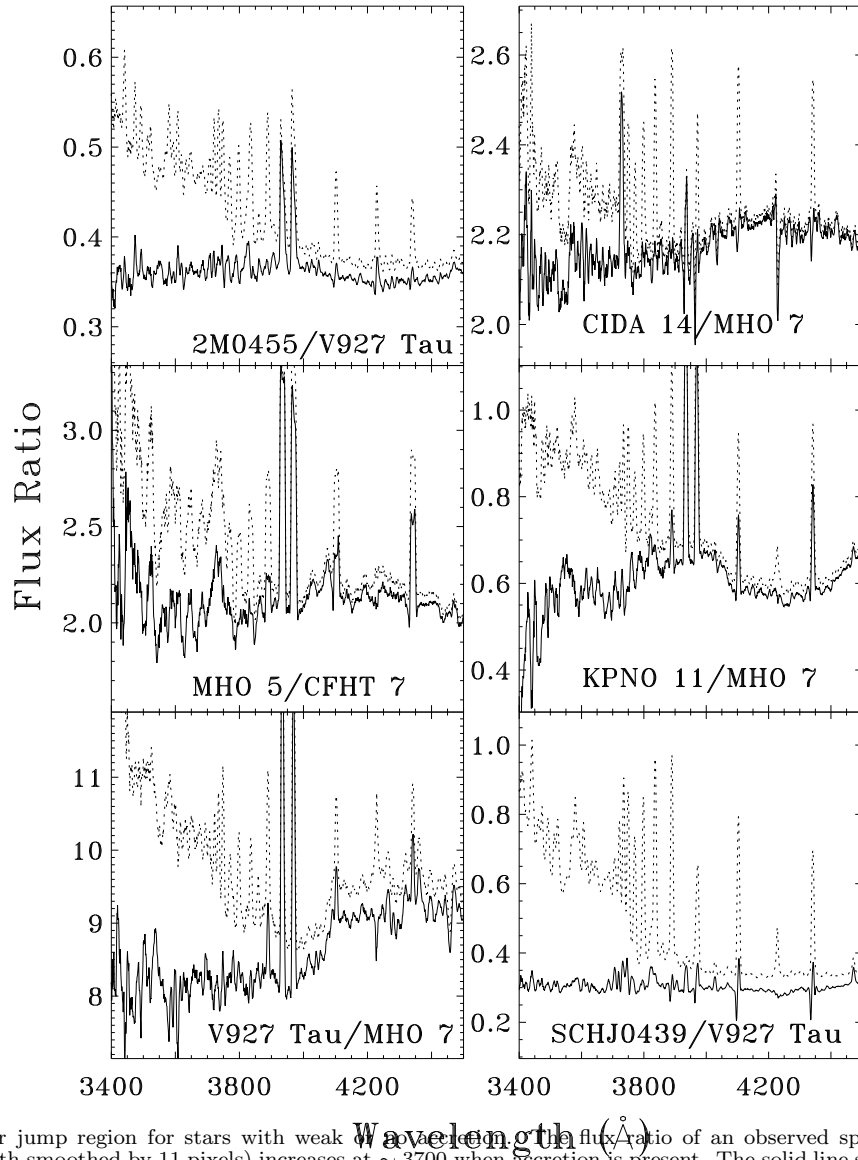


FIG. 6.— The Balmer jump region for stars with weak Balmer emission. The flux ratio of an observed spectrum to a photospheric template (dotted line, both smoothed by 11 pixels) increases at ~ 3700 when accretion is present. The solid line shows the same ratio, after subtracting excess Balmer line and continuum emission from the spectrum. For a perfect model and photospheric template, the residuals should be a line equal to the flux ratio with noise introduced from both the spectrum and photospheric template. Some excess Balmer continuum emission is seen from each source plotted here. The excess Balmer continuum emission from S0439+2336 is strong enough to be attributed to accretion. Fainter Balmer excess emission may be produced by either chromospheric activity or accretion.

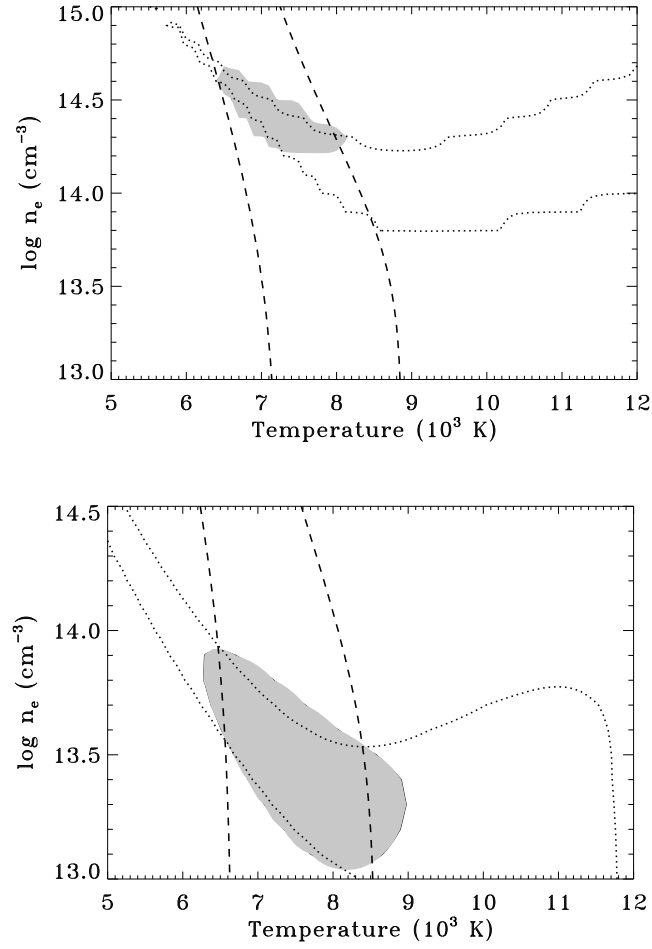
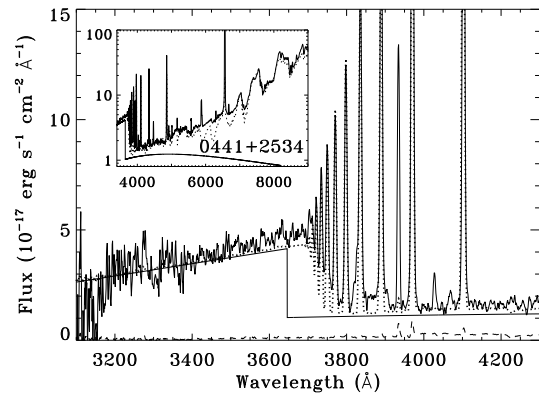
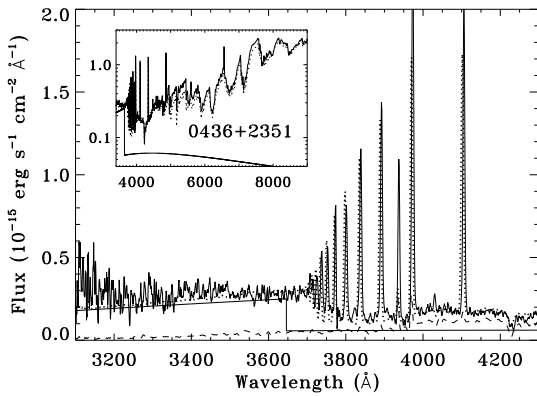
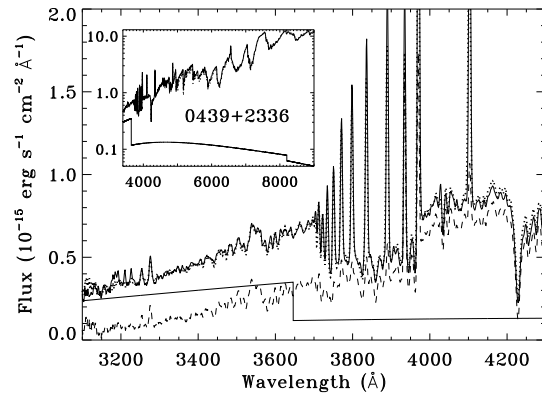
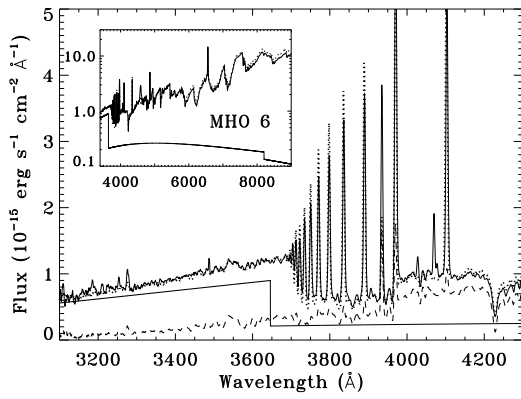
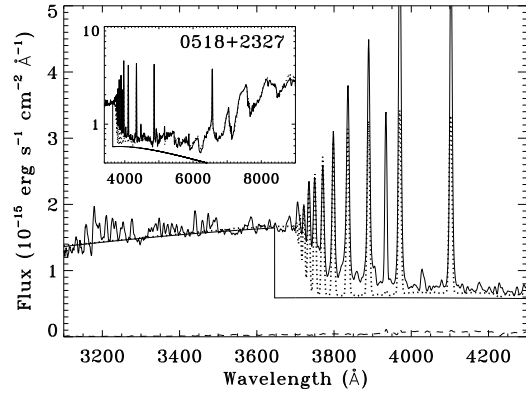
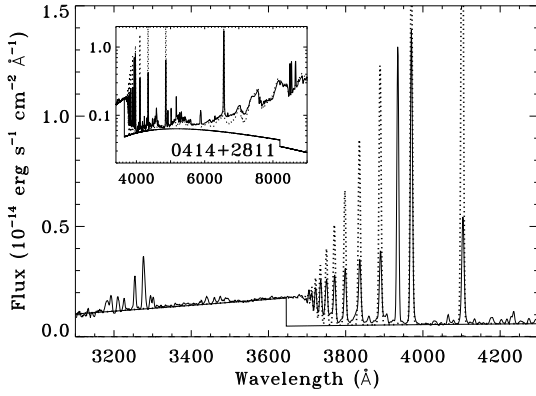
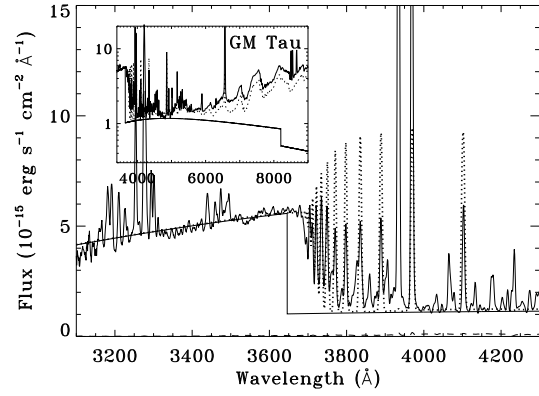
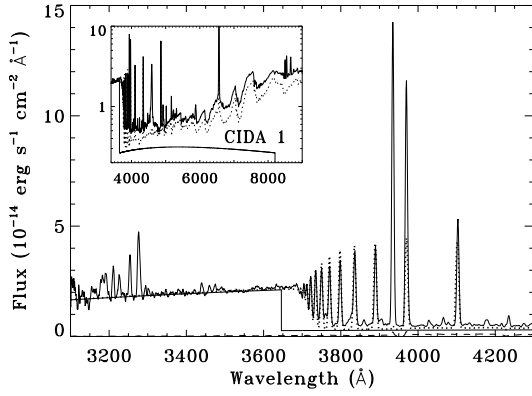
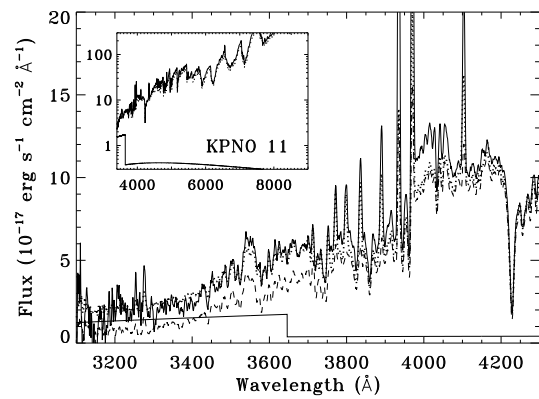
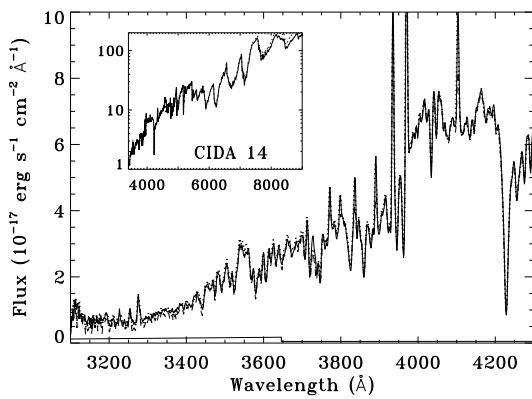
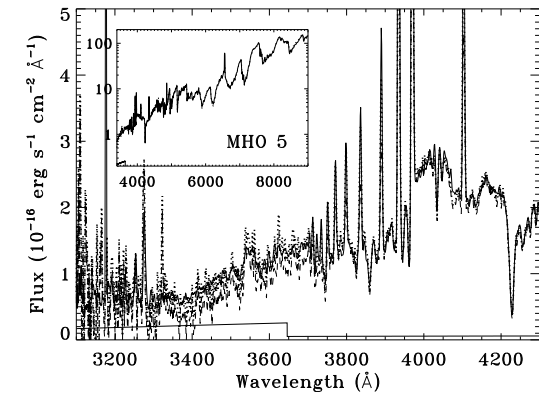
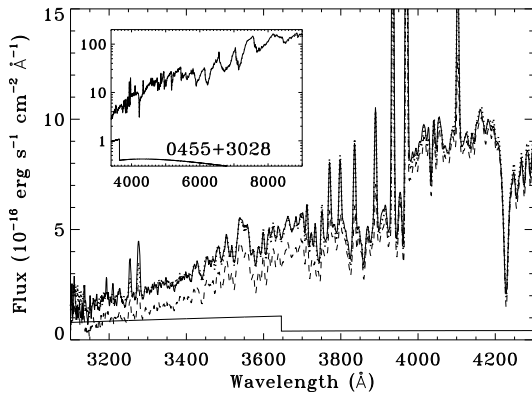
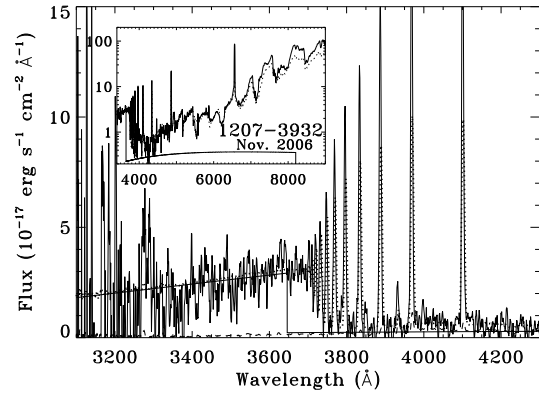
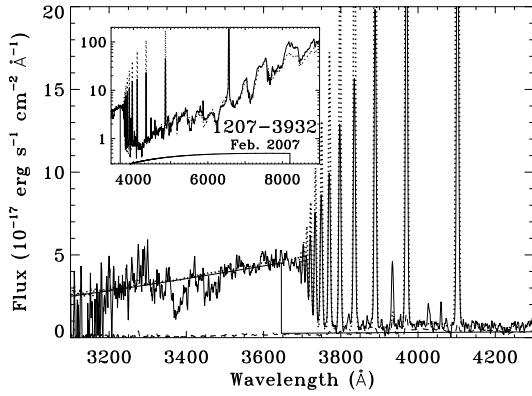
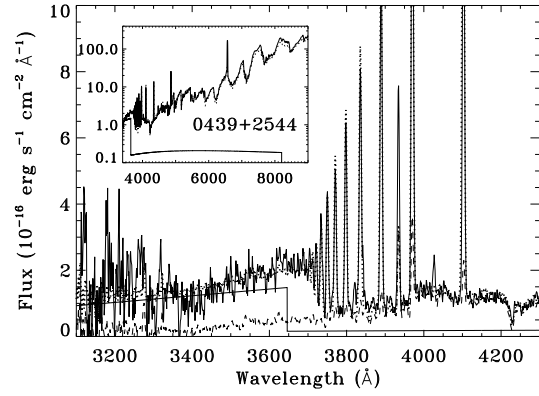
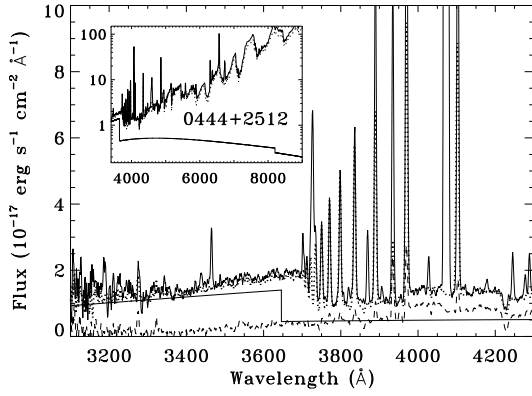


FIG. 7.— Contours of acceptable T and n_e for isothermal hydrogen slab model fits to the spectra of 2M0414+2811 (left) and 2M1207-3932 (right). The vertical contours that determine T are constrained by the slope of the Balmer continuum. The horizontal contours that determine n_e are constrained by the size of the Balmer jump. For 2M0414+2811 the acceptable values of T and n_e together differ from their intersection because they are only acceptable for different values of L .





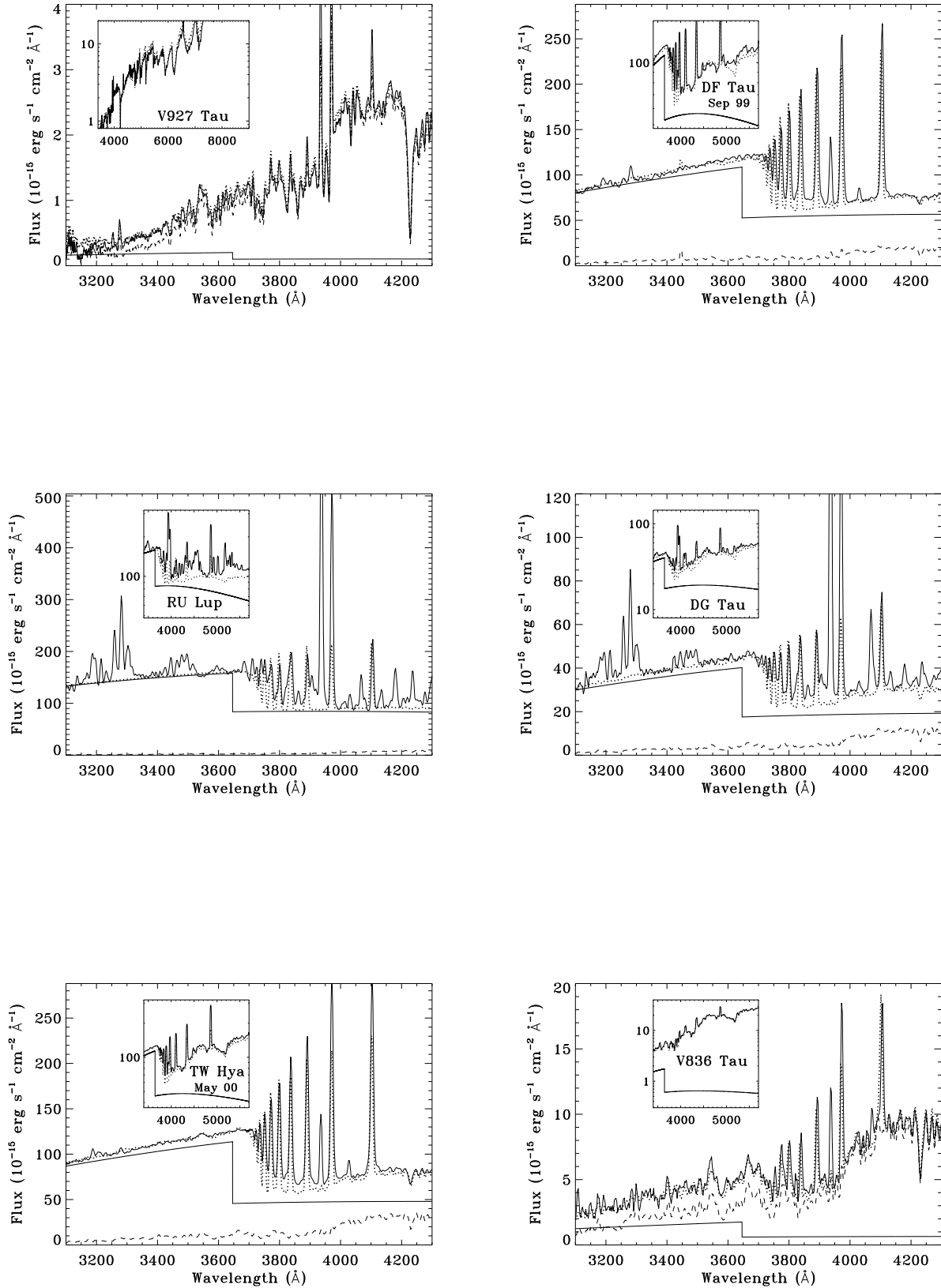


FIG. 8.— The observed emission (solid spectrum), corrected for reddening (Table 1), is fit with the combination of a photospheric template (dashed line, listed in Table 5 and not shown in the smaller panel) and a synthetic accretion spectrum from a slab model (light solid line, Balmer lines are not shown for clarity). The total fit is shown as a dashed line that overlaps the observed spectrum.

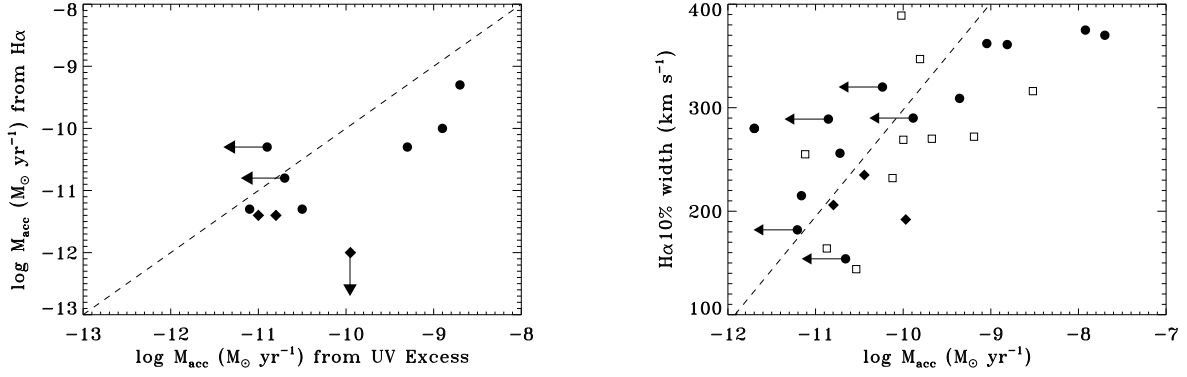
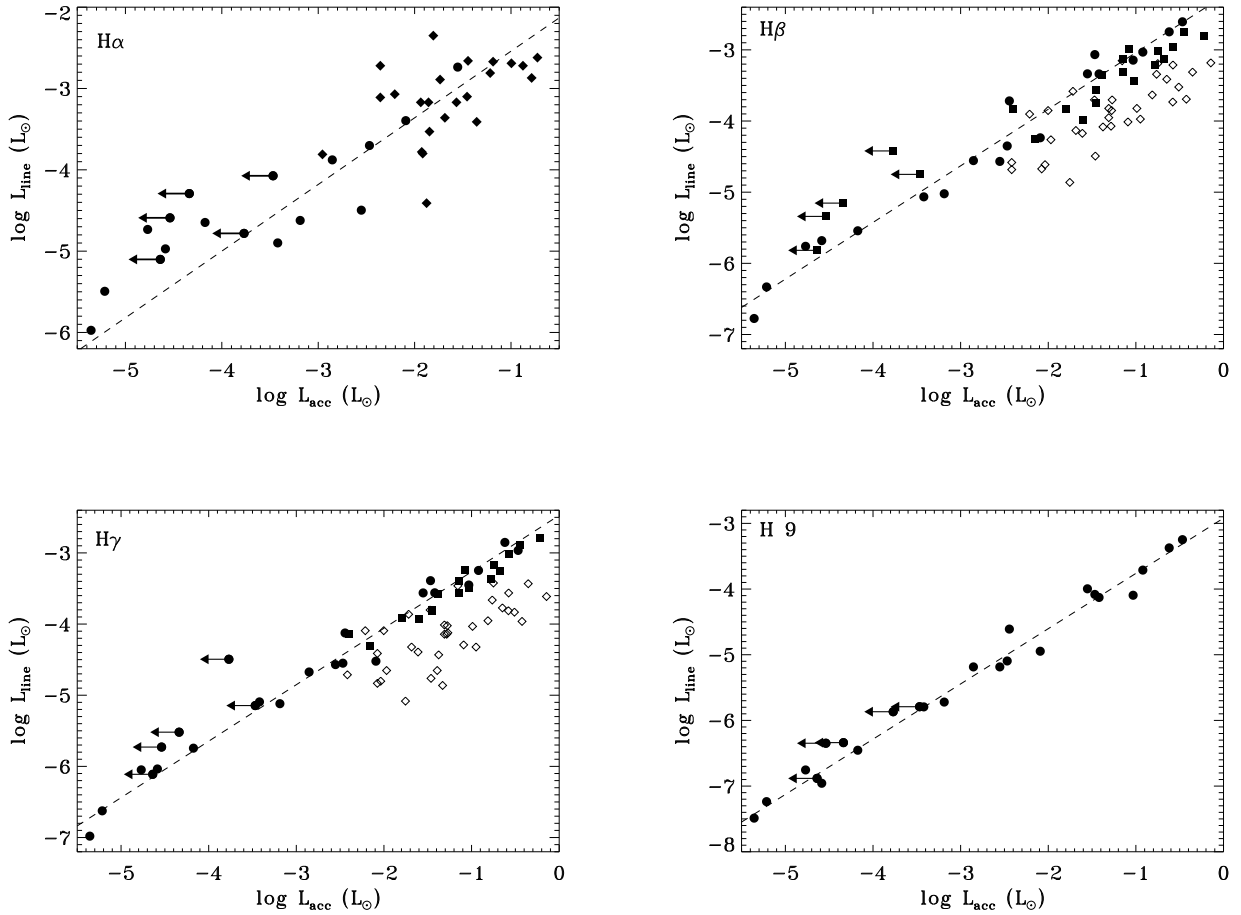
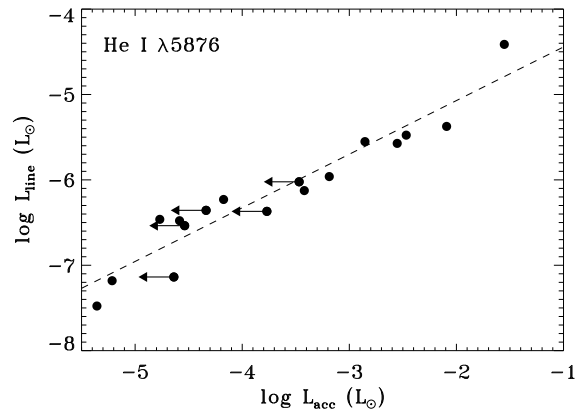
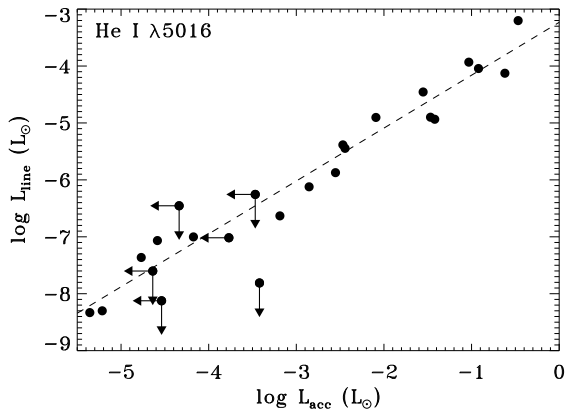
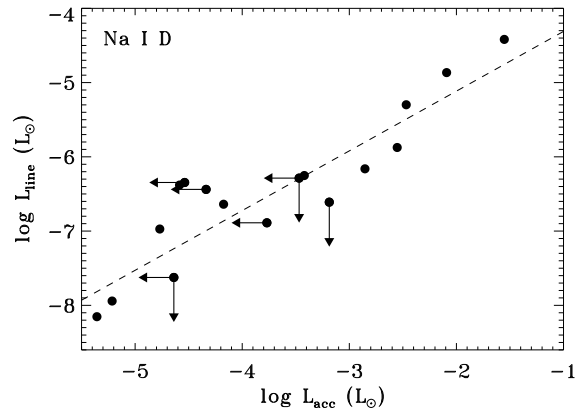
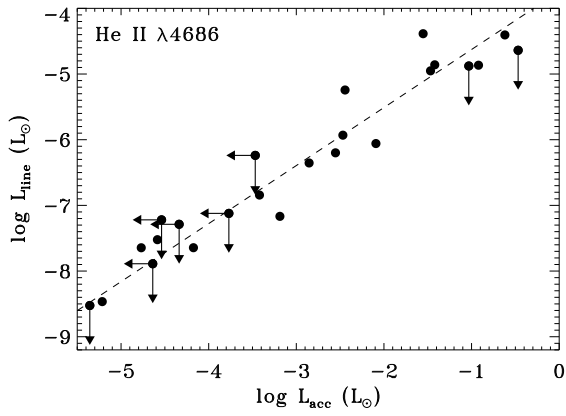
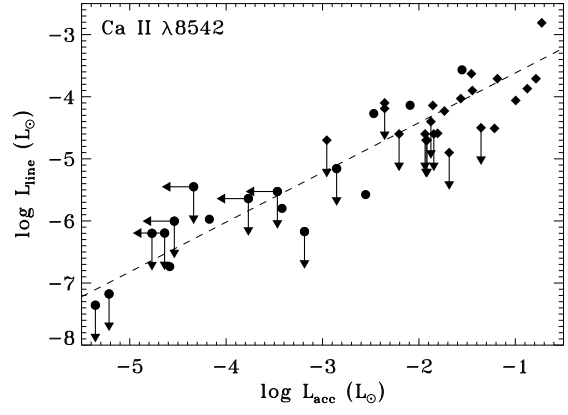
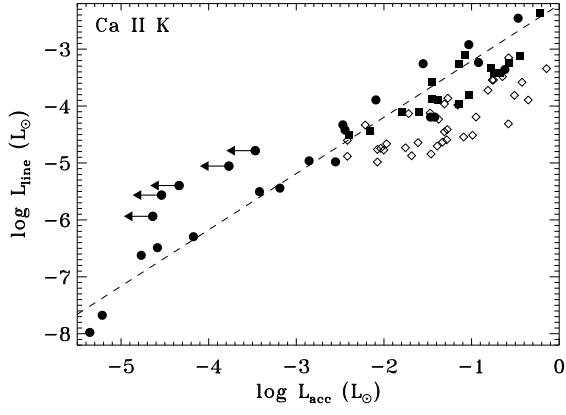


FIG. 9.— UV excess measure of \dot{M} versus non-simultaneous measurements of \dot{M} from models of the H α line profiles (left, from Muzerolle et al. 2000, 2003, 2005) and versus non-simultaneous measurements of the H α 10% width (left). The circles are accretors with \dot{M} measured from UV excess and the diamonds are accretors with \dot{M} measured from the V-band excess (Table 14) reported by Kraus et al. (2006). The dashed line on the left panel denotes where two accretion rate measures would be equal. The dashed line on the right panel denotes the \dot{M} –H α 10% width relationship calculated by Natta et al. (2004).





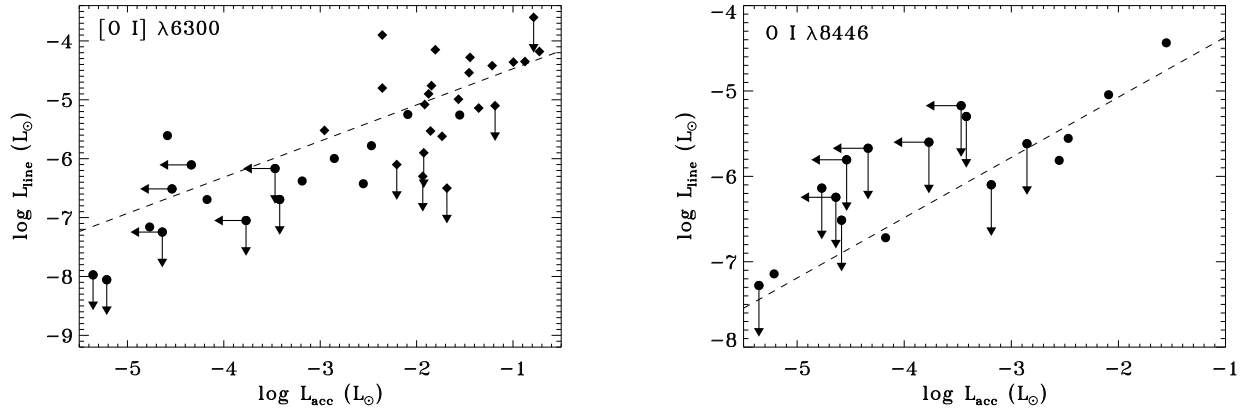


FIG. 10.— The relationship between selected line luminosities and the accretion continuum luminosity. The filled circles represent the accretors with strong excess Balmer continuum emission that is produced by accretion. The upper limits in L_{acc} are the five possible accretors, which have weak Balmer continuum emission that may be attributed to either accretion or chromospheric activity. We include results from Valenti et al. (1993, empty diamonds and corrected for the 140 pc distance to Taurus) and Gullbring et al. (1998, filled squares) for fits to the $H\beta$, $H\gamma$, and Ca II K line luminosities, and Hartigan et al. (2003, filled triangles) for fits to the $H\alpha$, Ca II $\lambda 8542$, and [O I] line luminosities. The dashed lines are linear fits to the data as described in §5.3 and Table 15.

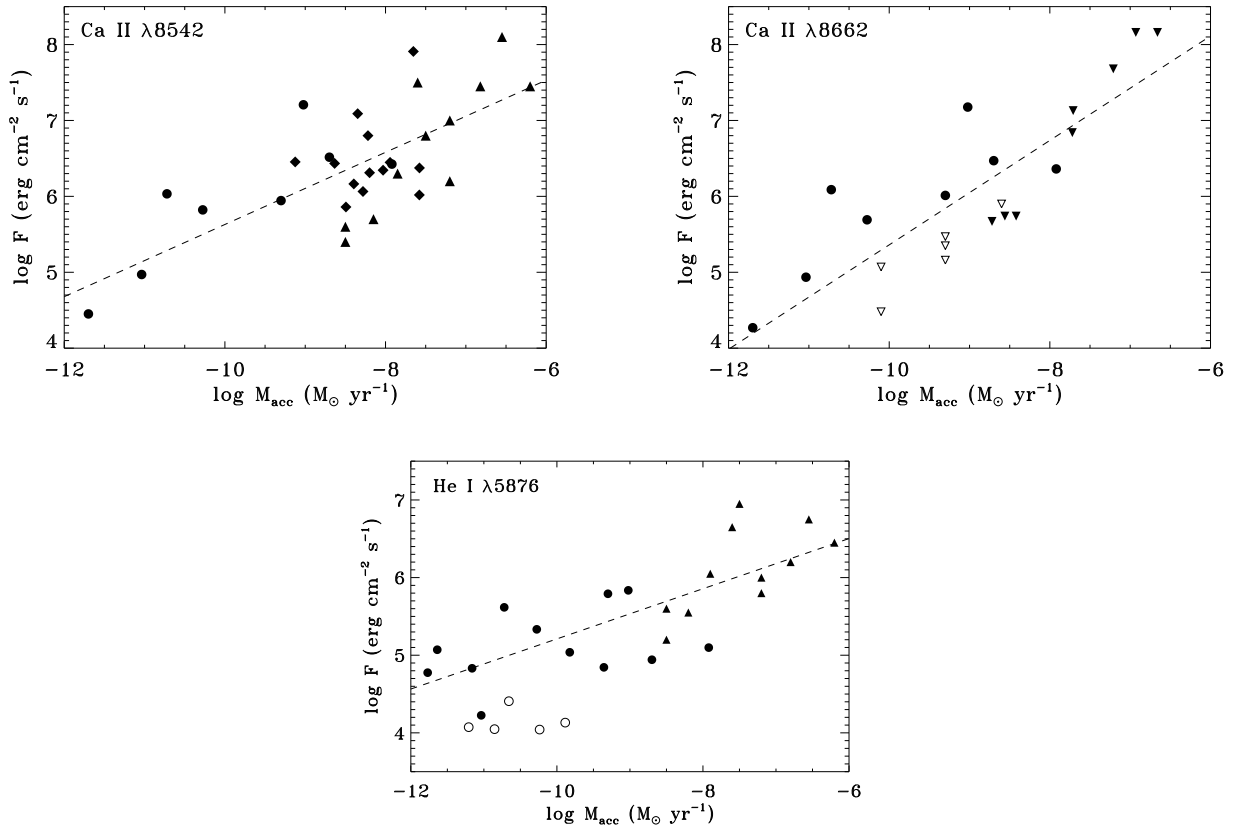


FIG. 11.— Ca II $\lambda 8542$ (upper left) and Ca II $\lambda 8662$ (upper right) line flux versus mass accretion rate. We compare our data (filled circles for accretors, empty circles for the five possible accretors) with that from Hartigan et al. (2003, filled diamonds for Ca II $\lambda 8542$), Muzerolle et al. (1998, filled triangles for Ca II $\lambda 8542$ and He I $\lambda 5876$) and Mohanty et al. (2005, upside-down triangles for Ca II $\lambda 8662$). The empty upside-down triangles on the upper right panel signify that the \dot{M} was measured by $H\alpha$ modelling and is multiplied by 5. The dashed lines in both panels show the best fit through the data.

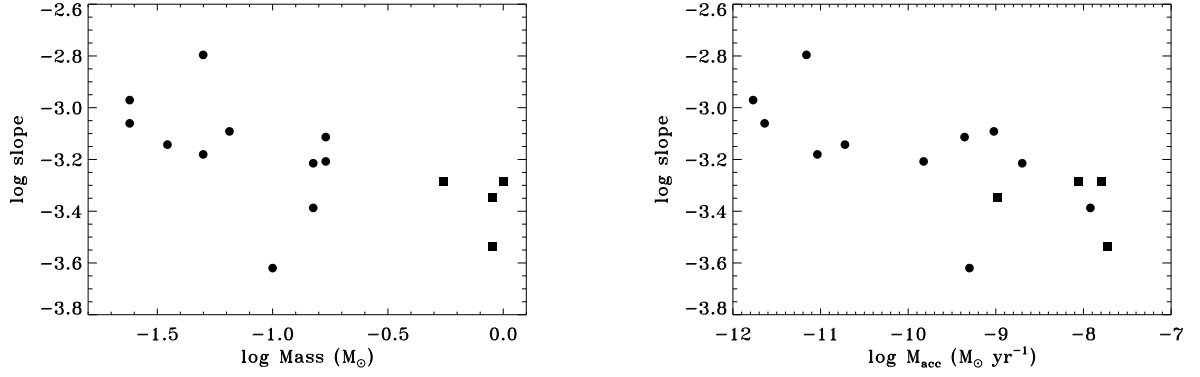


FIG. 12.— The slope of the Balmer continuum versus stellar mass (left) and \dot{M} (right). The circles are from our *Keck I*/LRIS data, the squares from *HST*/STIS G430L spectra. The slope of the Balmer continuum increases to smaller M and \dot{M} , suggesting that it is produced at cooler gas.

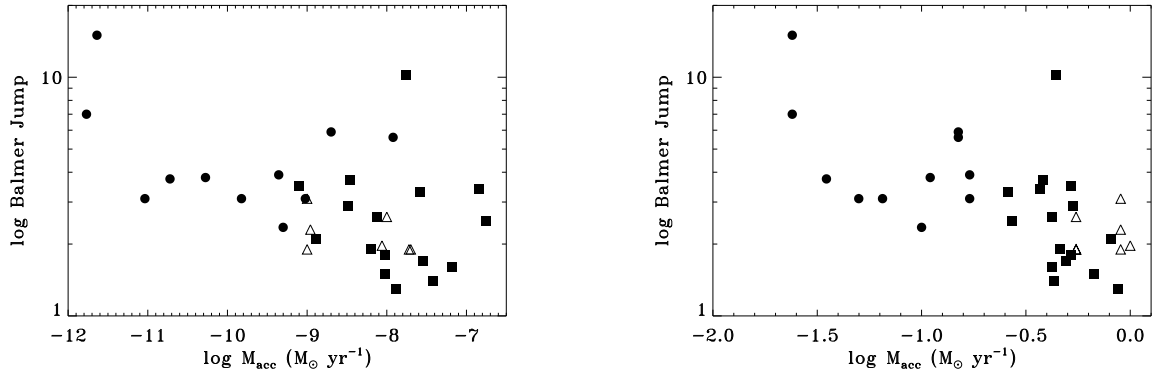


FIG. 13.— The Balmer jump versus stellar mass (left) and \dot{M} (right), as in Fig. 12. The squares are from Gullbring et al. (1998). The Balmer jump tends to increase to smaller M and \dot{M} , suggesting that the accretion continuum is produced in gas with a lower electron density.

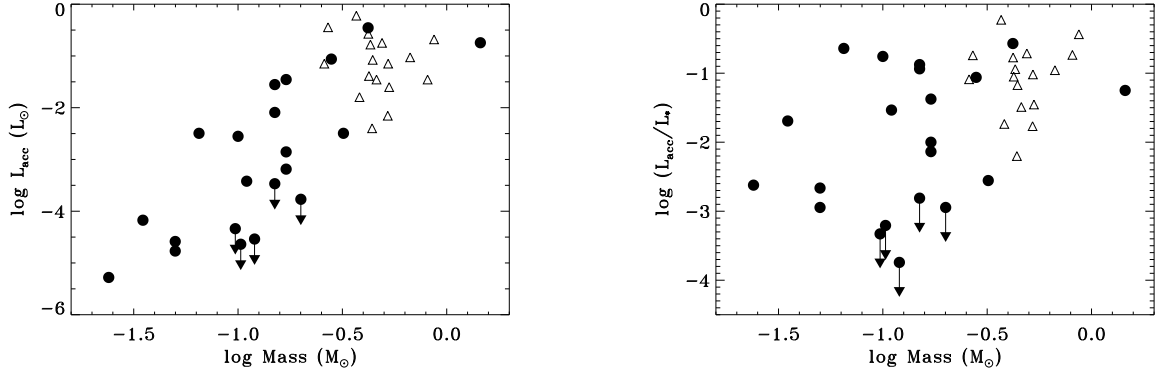


FIG. 15.— The relationship between mass and L_{acc} (left) and $\frac{L_{acc}}{L_{bol}}$ (right), with circles from our data and open triangles from Gullbring et al. (1998). The sensitivity of measuring L_{acc} and $\frac{L_{acc}}{L_{bol}}$ from the UV excess improves to lower masses.

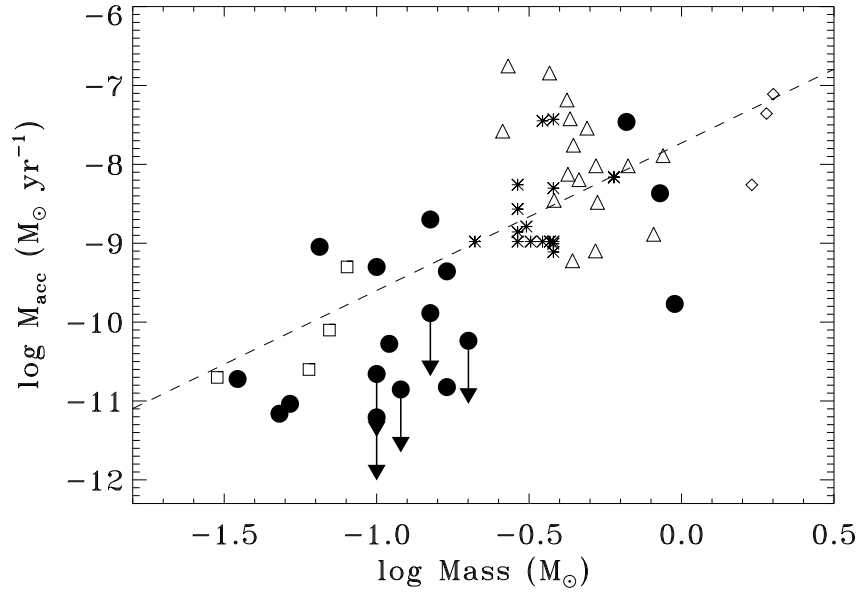


FIG. 14.— Mass versus mass accretion rate for Taurus members with $A_V < 2.5$ and measured accretion rates. The data plotted are \dot{M} measured from excess UV continuum emission in this work (filled circles), from excess UV continuum emission measured by Gullbring et al. (1998, open triangles), optical veiling measured by Hartigan & Kenyon (2003, asterisks), UV excess measured by Calvet et al. (2004, open diamonds), and $H\alpha$ profile modelling (open squares, multiplied by 5, Muzerolle et al. 2005). The dashed line shows $\dot{M} \propto 7.7 M^{1.87}$.